PHYSICAL REVIEW D VOLUME 35, NUMBER 12 15 JUNE 1987

Superconducting gravity gradiometer for sensitive gravity measurements. II. Experiment

H. A. Chan,* M. V. Moody, and H. J. Paik
Department of Physics and Astronomy, University of Maryland, College Park, Maryland 20742
(Received 1 July 1986)

A sensitive superconducting gravity gradiometer has been constructed and tested. Coupling to gravity signals is obtained by having two superconducting proof masses modulate magnetic fields produced by persistent currents. The induced electrical currents are differenced by a passive superconducting circuit coupled to a superconducting quantum interference device. The experimental behavior of this device has been shown to follow the theoretical model closely in both signal transfer and noise characteristics. While its intrinsic noise level is shown to be 0.07 $\mathrm{E\,Hz^{-1/2}}$ (1 $\mathrm{E} \equiv 10^{-9}\ \mathrm{sec^{-2}}$), the actual performance of the gravity gradiometer on a passive platform has been limited to 0.3–0.7 $\mathrm{E\,Hz^{-1/2}}$ due to its coupling to the environmental noise. The detailed structure of this excess noise is understood in terms of an analytical error model of the instrument. The calibration of the gradiometer has been obtained by two independent methods: by applying a linear acceleration and a gravity signal in two different operational modes of the instrument. This device has been successfully operated as a detector in a new null experiment for the gravitational inverse-square law. In this paper we report the design, fabrication, and detailed test results of the superconducting gravity gradiometer. We also present additional theoretical analyses which predict the specific dynamic behavior of the gradiometer and of the test.

I. INTRODUCTION

The equivalence principle prohibits distinction of "gravity" from "acceleration" by a *local* measurement. The same principle, however, implies that a sensitive *accelerometer,* or a *gravimeter,* can be used as an approximate detector of gravity in an environment where the platform accelerations are small. Thus, gravimeters, which measure absolute and relative magnitudes of the gravitational acceleration vector, usually from a stationary platform, have been employed as geophysical survey instruments.[1] This method of measuring gravity can be extended to a moving platform by independently determining and compensating for the platform accelerations with the aid of a geodetic navigation device such as the global positioning system (GPS) satellite network.[2] The latter measurement is clearly of a *global* nature.

An alternative, more direct, approach to a rigorous determination of the gravitational field is by means of a *gravity gradiometer,* which measures components of the tidal force or the Riemann tensor.[3] Here an *almost local* measurement is made by monitoring relative motions of proof masses separated by a short, but finite, base line. With the torsion balance as the predecessor, several advanced types of gravity gradiometers have been developed recently.[4]

The superconducting gravity gradiometer, to be discussed in this paper, has been developed with the primary motivation being to perform precise tests of gravitational theories in both terrestrial and space laboratories. A preliminary version of a null test of the gravitational inverse-square law has been carried out with this instrument.[5] While the instrument has served as a prototype for a three-axis superconducting gravity gradiometer[6] which is under construction, the system has undergone a thorough theoretical and experimental analysis to test the physics of the instrument. The results could easily be adapted to a more complicated device.

In paper I a detailed theoretical analysis of the current-differencing gravity gradiometer was presented. This paper (paper II) discusses the design, construction, and test results of the actual instrument. These test results demonstrate that the physical device is described by the theoretical model in great detail. In addition we discuss here the principle and operation of two elegant experimental techniques, which have been applied to the superconducting gravity gradiometer: (1) accelerometer mode calibration and (2) vibration isolation by means of pendulum action. Also, the error model of the instrument developed in paper I is extended and applied here to the specific instrument configuration chosen. Paper II represents an extension of the experimental work reported in Ref. 7.

The gravity gradient signal sought for is usually a small fluctuation over a relatively large background of the Earth's gravity and the seismic activity of the platform. Therefore, precise mechanical alignment of components and extreme stability of scale factors, as well as high sensitivity, are required for a practical gravity gradiometer. Advantages of a superconducting instrument in these regards have been pointed out in paper I. In this paper we show how quantum-mechanical properties of superconductors are utilized specifically, along with careful mechanical design, to meet the challenge of constructing a highly sensitive gravity gradiometer.

Notations employed in paper II follow those of paper I, unless explicitly stated otherwise.

II. DESIGN AND FABRICATION OF THE SUPERCONDUCTING GRAVITY GRADIOMETER

A. Gradiometer hardware

The gradiometer consists of two accelerometers, each with a proof mass, a suspension structure, and sensing coils. The suspension structure consists of mechanical springs which confine the proof mass motion along the desired direction.

A folded cantilever suspension has been employed to produce a suspension with a linear spring constant which is weak, in the direction of motion, yet relatively rigid for other degrees of freedom. This type of suspension was suggested by Daniel DeBra at Stanford University and has been employed in the displacement-differencing gravity gradiometer.[8] The design contains eight folded cantilevers in an $\bar{8}m$ symmetry (to be defined later) to suspend the proof mass at the center (Fig. 1). Each cantilever consists of three joined diaphragm strips, of length l_s and thickness t_s, formed at the bottom of one radially oriented groove. The "fold" of the cantilever is at the radially outward ends of the strips. The radially inward ends of the strip are the ends of the spring. The middle strip of width b_s holds the center moving mass. The other two strips of width $\frac{1}{2}b_s$ link to a bulk mass which is a solid continuation of the outer rim of the suspension. This design allows the cantilevers to undergo nearly *pure bending* without stretching in order to achieve linearity in the spring constant. There are four folded cantilevers on each of two parallel planes with $2\pi/8$ rotation plus inversion symmetry ($\bar{8}m$ symmetry). Thus, motion of the center mass is linearized along the cylindrical axis.

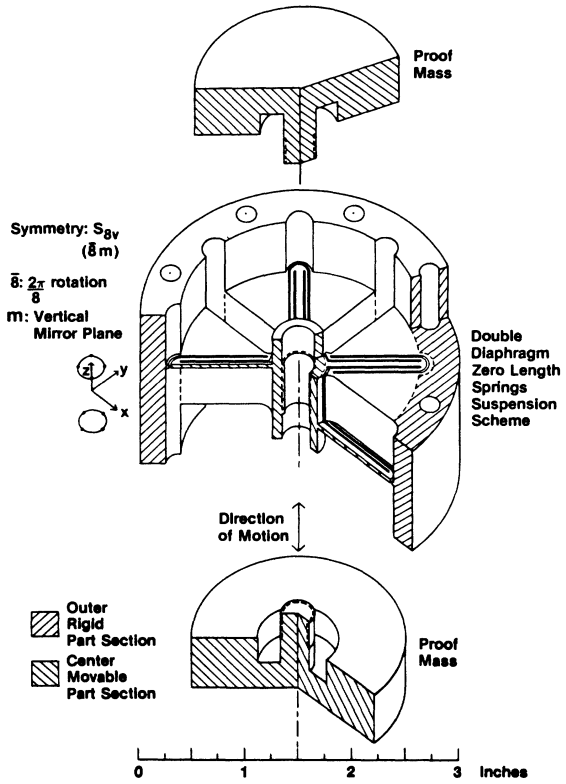

FIG. 1. A cut-away view of proof mass suspension.

The entire suspension structure is machined out of a *single* piece of niobium (Nb) in order to ensure mechanical precision and to obtain a high quality factor of resonance. Eight grooves, four from each side, are first milled out, leaving a thick diaphragm at their opposite sides. The metal is then stress relieved at 800 °C. The grooves are then electric-discharge machined (EDM) to thicknesses of (0.35 ± 0.01) mm. Next, the suspension structure is chemically polished with a mixture of hydrofluoric acid (HF), phosphoric acid (H_3PO_4), and nitric acid (HNO_3) in an ultrasonic cleaner. After the polishing, the Nb is partially recrystallized by annealing in a vacuum oven at 1100 °C. The designed pattern of slots is then cut with a wire EDM. Finally, the finished proof mass suspension structure is chemically polished again.

The center moving mass of the suspension is loaded with two mushroom-shaped Nb masses which screw into opposite ends to form one proof mass. This added load serves to increase the mass m_k, lower the suspension frequency f_{kM}, and provide two superconducting planes which modulate the inductances of the sensing coils. The mechanical suspension frequency of the proof mass is derived from the formula for a loaded beam and is given by

$$\omega_{kM}{}^2=(2\pi f_{kM})^2=\frac{E_s b_s t_s{}^3}{2(m_k/n_s)l_s{}^3}\ . \tag{1}$$

Here $E_s=1.03\times10^{11}$ N m^{-3} is the Young's modulus of Nb and $n_s=8$ is the number of springs used. Also, $t_s=0.35$ mm, $l_s=19$ mm, $b_s=2.5$ mm, and $m_k=0.40$ kg, giving $f_{kM}\simeq20$ Hz.

The sensing inductors are "pancake-shaped" coils wound out of thin (0.076 mm in diameter) Nb wire in a single layer. The coil form is made of machinable glass ceramic, Macor (Corning Glass Works, Corning, New York), whose thermal expansion coefficient matches closely with that of Nb down to cryogenic temperatures. A continuous length of insulated Nb wire is wound uniformly on the flat coil form in a spiral shape. Low viscosity, transparent, TRA-CAST BB3002 epoxy (TRA-CON, Inc., Medford, Massachusetts) is used to bond the Nb wire. The coil winding procedure used here is a modification of that described in Ref. 9.

Two such pancake coils are located next to the two plane surfaces of the proof mass in each accelerometer. To a high accuracy, the inductance for each pancake coil,

$$L(t)=\mu_0 n_L{}^2 A_L[d+x(t)]\ , \tag{2}$$

changes linearly according to its average spacing from the superconducting ground plane, and is insensitive to any rocking or transverse modes of the proof mass. The coil forms are mounted rigidly on Nb holders using Nb screws and GE 7031 varnish. The two Nb holders are mounted rigidly to the outer rim of the proof mass suspension using titanium (Ti) screws to form a shielded accelerometer. Ti is closely matched in thermal expansion coefficient

with Nb. The spacing between the coil and the proof mass is adjusted by adding Nb spacers cut out of Nb sheet. Parallelism between the coil and proof mass surface is desirable to allow the use of a small spacing between them.

Two accelerometers are mounted on the opposite faces of a precision Ti (Ti V_4 Al_6 alloy) cube to form a single-axis gradiometer (see Fig. 2). The surfaces of the cube have parallelism and orthogonality within 50 ppm. The same degree of parallelism is kept for the mating surfaces of all the gradiometer parts. The Ti material at the center cube is continued down to an aluminum-to-titanium joint. An aluminum (Al) base is tight fitted onto the Ti at room temperature. Differential contraction tightens the joint further as the assembly is cooled down. A similar joint is made at the upper end. The base line of the gradiometer, which is defined by the distance between the centers of mass for the two proof masses, is $l=0.16$ m.

For most of the tests reported in this paper, one triagonal axis of the mounting cube is aligned with the vertical, as is shown in Fig. 2, so that the sensitive axis of the gradiometer is tilted by an angle

$$\theta_u=\arctan\sqrt{2} \tag{3}$$

from the vertical. This "umbrella orientation" has the advantage of allowing measurements in three orthogonal directions to be made by rotating the gradiometer around the vertical axis by 120° increments. The fact that the large dc gravity bias is matched along the sensitive axes is an important scientific reason to prefer this orientation when a careful three-axis measurement is called for. The above procedure has therefore been used for the null test of the gravitational inverse-square law,[5] which will be discussed in Sec. VI.

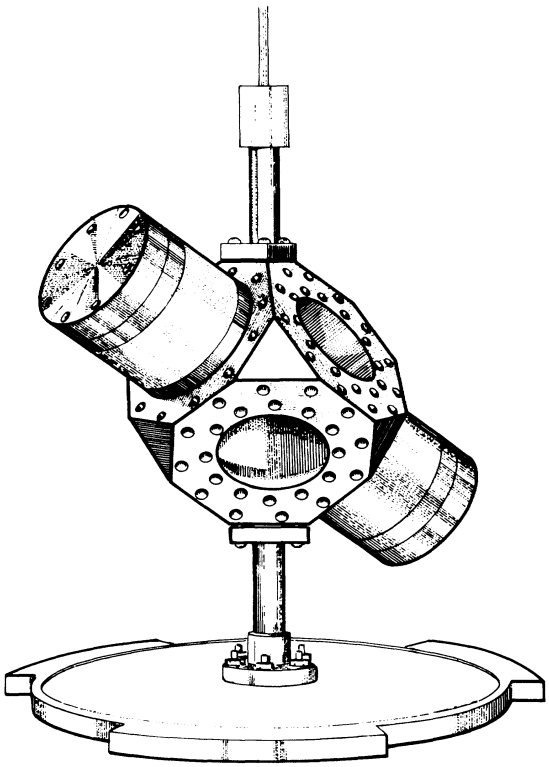

FIG. 2. A perspective view of the single-axis gravity gradiometer in umbrella orientation.

B. Superconducting circuitry

The superconducting circuit for the gradiometer is shown in Fig. 3. L_{1a},L_{1b} and L_{2a},L_{2b} are pancake coil inductors for the two proof masses, m_1 and m_2, respectively. S_{1a}, S_{1b}, S_{2a}, S_{2b}, and S_I are current leads from the current supply outside the cryostat. H_1, $H_{1\delta}$, H_2, and $H_{2\delta}$ are shielded heat-switch resistors. When currents are sent through these resistors, appropriate sections of the superconducting path are switched into their normal state. $R_{1\delta}$ and $R_{2\delta}$ represent extremely low-resistance current paths (3×10^{-9} Ω). L_i is the input inductor of the SQUID (superconducting quantum interference device) amplifier. $L_{\rm I}$ and $L_{\rm II}$ are, respectively, the primary and secondary of a high coupling transformer.

The current I_1 can be stored in $L_{1a}+L_{1b}$ by turning H_1 on and then off while the current is sent across S_{1a} and S_{1b}. The inductance $L_{1a}+L_{1b}$ can be determined by measuring the flux trapped in it after a known current has been stored. The flux is measured by the time integral of the voltage decay across the leads S_{1a} and S_{1b} as H_1 is turned on. This method has been described in Ref. 9. There is also a heat switch H_S, between $L_{\rm II}$ and L_i that will be turned on in all operations involving current changes. This heat switch serves to protect the Josephson junction of the SQUID ring against any surge current induced in the input coil L_i. The currents I_1 and I_2 in the two sensing loops can be fine-tuned by letting the stored flux leak very slowly across an ultra-low-resistance path after a section of the superconducting path has been turned normal. If the heat switch $H_{2\delta}$ is turned on, the current I_2 in $L_{2a}+L_{2b}$ will decay across $R_{2\delta}$ with a decay time $\tau=(L_{2a}+L_{2b})/R_{2\delta}\simeq3\times10^4$ sec, which is extremely long. This current will rise or decay even more slowly if a second current, slightly greater or smaller than I_2, is being sent across the leads S_{2a} and S_{2b} while $H_{2\delta}$ is kept on. An additional current i_1 can be added in the loop formed by a parallel combination $L_{1a}//L_{1b}$ as in Eq. (6) and L_I (see Fig. 3 of paper I) by turning both $H_{1\delta}$ and

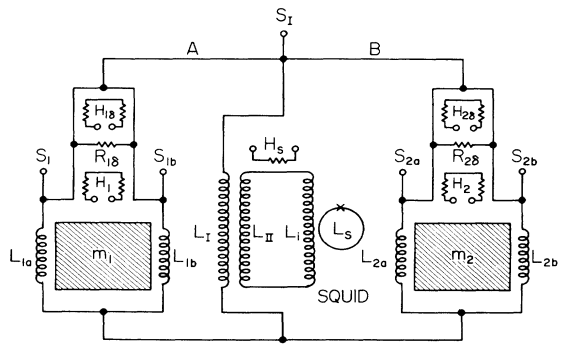

FIG. 3. The superconducting circuit for the gravity gradiometer.

$H_{2\delta}$ on and then off while a current is sent across S_I and either S_{1a} S_{1b}. The decay of I_1 and I_2 during the time required to store i_1 is negligible because of the long decay time τ. The directions of these persistent currents are as defined in Fig. 3 of paper I.

The superconducting circuit is shielded inside Nb. The outer surfaces of the Nb holders for sensing coils are shielded with additional Nb covers to form junction boxes. Circuit components such as superconducting joints, a superconducting transformer, shielded heat-switches, and ultra-low-value resistors are mounted in these junction boxes.

The superconducting joints and transformers are similar to those used in Refs. 9 and 10. A pair of Nb lead wires to be joined are twisted together, wrapped around a brass screw, sandwiched between two Nb sheets, and clamped together under a brass washer. Joints made this way consistently have critical currents in excess of 3 A through several thermal cycles.[11] The transformer makes use of a Nb sheet to guide the magnetic field through the primary and secondary coils.

Shielded heat switches are made with a small cylindrical Nb cup which shields the superconducting circuit from the noise of the heater resistor. The heater element is a small 500-Ω Allen-Bradley resistor which is glued with GE 7031 varnish inside the Nb cup. Shielding from the resistor is continued with superconducting lead-tin (PbSn) tubing which starts from inside the Nb cup to enclose the lead wires of the heater. The sections of Nb wire to be affected by the heat switch are wound noninductively on the outside surface of the Nb cup and are glued with the GE varnish. The cup is then glued on a piece of Fiberglas which is held rigidly inside the junction box. The Nb wires from the heat switches are heat sunk to the Nb mass of the junction box.

The shielding of the heat switches provides significant improvement in preventing electrical pickup and rf interference at the input of the SQUID amplifier. The shielding has a drawback, though, in possessing a higher heat capacity which prolongs the response time of the heat switch. By making the heat switch compact, we managed to obtain an on/off response time of about 0.2 sec with 4 mW supplied to the heater.

The ultra-low-resistance heat switch makes use of the radial conduction across a very thin cylindrical wall of copper. We simply solder two lengths of copper-clad Nb wires together with PbSn solder. The copper coating gives extremely low resistance between the superconducting PbSn on its outside wall and the Nb wire inside. The resistance between the two Nb wires comes from two such resistors connected in series. This resistance is given by the formula

$$R_\delta = \frac{\rho_{\mathrm{Cu}}(4.2\ \mathrm{K})}{\pi l_{\mathrm{Cu}}} \ln \frac{r_{\mathrm{Cu}}}{r_{\mathrm{Nb}}} \ . \tag{4}$$

We used Nb wire of diameter $2r_{\mathrm{Nb}}=0.128$ mm with copper coating which gives an overall diameter of $2r_{\mathrm{Cu}}=0.166$ mm. The resistivity of copper at 4.2 K is $\rho_{\mathrm{Cu}}\simeq 10^{-9}$ Ω m. Therefore, when a wire of length $l_{\mathrm{Cu}}=10$ mm is used, we obtain $R_\delta \simeq 10^{-8}$ Ω. This resistance has been verified in a decay time measurement of magnetic flux. The other two ends of the copper-clad Nb wires have their copper layer removed with concentrated HNO_3 so that superconducting joints can be made there. In the rest of the superconducting circuit, Nb wires without copper coating are used to avoid ac losses due to eddy currents.[9]

In the original circuit used for tests, an additional SQUID was coupled to the superconducting circuit to measure the common acceleration simultaneously. Two identical superconducting transformers were inserted into the paths that connect the two sensing loops to L_1 (A and B in Fig. 3), with one on each accelerometer side. The primaries of these transformers completed the gradiometer circuit. Their secondaries were connected in series with the input coil of the second SQUID. The current induced in this loop was proportional to the sum of the signal currents from the two accelerometers, permitting a simultaneous readout of the common acceleration in the "gradiometer mode." Although such a readout is useful for error compensation and active vibration isolation,[12] we have omitted, for simplicity, this additional circuit in the later tests in favor of the basic circuit shown in Fig. 3.

III. CONSTRUCTION AND PERFORMANCE OF TEST APPARATUS

A. Mechanical and thermal design of experimental space

The superconducting gravity gradiometer is operated in a very quiet cryogenic vacuum space with a stable temperature. A low boil-off liquid-helium (He) Dewar was designed and constructed with great care. Radiation shields with superinsulation are used in preference to a liquid-nitrogen (N_2) shield, because boiling liquid N_2 is a much noisier source of vibration than boiling liquid He. Pressure pads are sandwiched near the bottom of the Dewar between the Fiberglas inner tube and the sturdy outer Al wall. The relatively weak inner tube is then damped against swinging motions. The inside dimensions of the Dewar are 0.378 m in diameter and 1.778 m in height.

A low heat-leak insert has been constructed to complement the Dewar. An Al vacuum can is supported by three equally spaced Fiberglas tubes and one center Fiberglas tube which permits access to the vacuum space from the Dewar top. The vacuum space is 0.33 m in diameter by 0.61 m in height. The can remains totally submerged for one week with 60 liters of liquid He. A long hold time of He is needed for an uninterrupted operation of sensitive measurements. The low boil off rate is also important for lower boiling noise from the He and for lower thermal drift of the experiment.

For most of the experiment the gradiometer assembly was suspended inside the vacuum by means of a Fiberglas rod from the room temperature end of the Dewar insert. All the lead wires are heat sunk in liquid He before they enter the vacuum space through specially made feedthroughs. In this setup, long-term temperature variations of the gradiometer assembly over many weeks average about 10 mK. In a time scale of several hours, the temperature variations are within the 2-mK resolution of a

germanium (Ge) resistance thermometer mounted on the gradiometer. The heat capacity of the gradiometer and the weak thermal coupling to the He bath form a low-pass filter for the temperature fluctuations between the gradiometer and the He bath. The response time is estimated to be on the order of minutes.

B. Electromagnetic shielding

External magnetic field fluctuations and electrical pickup can produce a high noise level in comparison with the very weak gravitational force. rf interference will also deteriorate the noise performance of the rf SQUID and can unlock the SQUID feedback loop. The first stage of magnetic field isolation is provided by a double wall μ-metal shield which surrounds the cryostat. Two additional superconducting stages of magnetic shielding are provided by a 1-μm lead (Pb) film evaporated on the inner wall of the vacuum can, and by the Nb body of the gradiometer itself. Also, the Al walls of the Dewar and the vacuum can aid in shielding high-frequency electromagnetic radiation.

The success of the electromagnetic shielding is evidenced by the achievement of the optimum SQUID amplifier noise when the SQUID input is coupled to the gradiometer at full sensitivity. The magnetic shielding has also been tested when the gradiometer is balanced. A magnet producing 600 G being flipped just outside the Dewar produced a response less than an equivalent flux change of 2×10^{-3} Φ_0 or 4×10^{-18} Wb at the SQUID input.

Each current lead for storing a supercurrent has an inductive choke inside the vacuum can. The choke is a high-impedance path to attenuate the electrical noise that the wire can pick up outside the Pb shield and especially outside the Dewar. The other leads pass through two stages of rf filters, one inside the Pb shield and the other outside it. The outside one is an *RC* low-pass filter with the manganin wire down the Dewar providing the resistance and the inside one is a capacitor in parallel with the load.

C. Vibration isolation

Vibration proved to be the most troublesome source of noise. The test of the gradiometer has therefore been conducted in a deep-underground laboratory, which is secluded from the traffic of people. The most critical noise data have been obtained in the evenings to minimize the mechanical and electrical disturbances of the experiment. In spite of these precautions, the gradiometer required careful mechanical isolation from the environment.

The vibration isolation system consists of a three stage low-pass filter schematically shown in Fig. 4. The gradiometer assembly is suspended by a Fiberglas rod and a length of latex rubber tubing in vacuum which form the first stage of vibration isolation. The vacuum is extended above the top of the Dewar insert by means of a thick-wall Plexiglas tube. The rubber tubing inside this Plexiglas tube hangs from a connecting rod which is attached to a massive brass plate that seals with the Plexiglas at the top. The height of the connecting rod can be adjusted

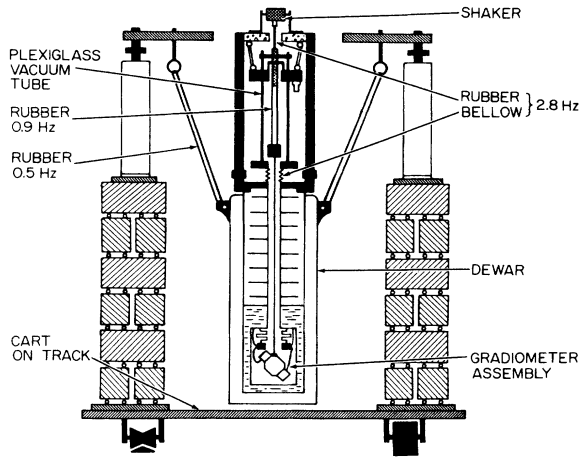

FIG. 4. Three-stage vibration isolation system.

from outside the vacuum so that the gradiometer can be lowered to the bottom of the vacuum can to short out the filter. When the gradiometer is suspended by the rubber tubing, the vertical resonance frequency is 0.9 Hz.

The Fiberglas and rubber also give *wideband isolation* from *tilt noise.* The gradiometer suspended by a long Fiberglas rod constitutes a pendulum. A natural property of a pendulum is its tendency to align itself along the direction of gravity. The gradiometer is therefore decoupled from a crucial error source: the *ground tilt,* which would cause an error signal due to modulation of Earth's gravity for a hard-mounted gradiometer.

Another important property of the pendulum is that the mass at the end of the rod is under a two-dimensional "free fall" in the horizontal plane. An accelerometer mounted on the pendulum bob therefore cannot experience any horizontal acceleration relative to the platform to the first order. A gravity gradiometer can, however, couple to the angular velocity and the angular acceleration which result from the pendulum response to the horizontal acceleration (see Sec. V and Appendix A for detailed discussions of the pendulum action). The net effect of the pendulum action for the *horizontal vibration* is that of a *low-frequency filter,* in series with a wideband attenuator.

Additional resonant modes of the suspension structure can deteriorate vibration isolation at the resonance peaks. In spite of these limitations we have chosen the pendulum suspension for the gradiometer because of its isolation characteristic for low-frequency horizontal acceleration and its simplicity in construction. The pendulum frequency (swinging mode) is approximately 0.3 Hz and the rubber tubing gives a torsional mode at 0.08 Hz. In addition, the massive gradiometer suspended by the long and therefore bendable Fiberglas rod gave a troublesome high-Q peak at 2.5 Hz. This peak was the result of a rocking mode of the gradiometer assembly around a horizontal axis.

The massive brass top of the Plexiglas column is suspended with a set of rubber tubings. The bottom of the Plexiglas column is connected to the top of the Dewar insert by a flexible vacuum bellows. The rubber tubing

and this bellows form the second stage of the filter with a vertical resonance frequency of 2.8 Hz. This filter can be shorted out by connecting clamps across the bellows.

The third stage of the filter is formed by three sets of rubber tubings that lift the Dewar off the floor. The Dewar is suspended from a framework by these rubber tubings and has a vertical resonance frequency of 0.5 Hz and a swinging frequency of 0.3 Hz. The upper joints of the rubber tubings in this suspension are adjustable so that the Dewar can be leveled. Again, this filter can be eliminated lowering the Dewar to the cart.

The advantages of using latex tubing as a passive filter are its high elasticity and low Q. A latex tubing of initial length l_i can be extended to a final length l_f which is a few times l_i. The cross-sectional area will decrease from A_i to $A_f = A_i(l_i/l_f)$ in order to keep the volume constant. We assume that the modulus of elasticity is approximately constant even with such large extension. One can easily show then that the vertical resonance frequency is

$$f = \frac{1}{2\pi}\left[\frac{g_E}{l_f - l_i}\right]^{1/2}\left[\frac{l_i}{l_f}\right]^{1/2}, \tag{5}$$

where l_f is the new length determined by gravity g_E acting on the load. The factor $(l_i/l_f)^{1/2}$ corrects for a change in the cross-sectional area as the rubber elongates. By having large extension $l_f - l_i$, a low resonance frequency is obtained. The low Q provided self-damping of the own resonance of the filter. Our latex tubing suspending the gradiometer in vacuum has $Q \simeq 10$.

The disadvantages of rubber are in relaxation and drift which worsen as the latex extends. A compromise is to keep $l_f \lesssim 2l_i$. We used $l_f \simeq 1.6 l_i$ for the rubber inside vacuum. Over a period of three months under load, it stretched by an additional 3 cm.

IV. GRADIOMETER PARAMETER MEASUREMENTS AND CIRCUIT OPTIMIZATION

A. Determination of geometric asymmetry

The main asymmetries between the two component accelerometers in a gradiometer come from the spacings of the sensing coils and mechanical spring constants. A high degree of matching for these parameters was not attempted because the mismatch can be compensated for by supercurrents. As can be shown from Sec. III of paper I, the low-frequency common mode balance condition in the small stored current limit with only two currents I_1 and I_2 reduces to

$$\frac{L_{2b}//L_{2a}}{L_{1b}//L_{1a}}\frac{{\omega_{2M}}^2}{{\omega_{1M}}^2} = -\frac{I_2}{I_1}, \tag{6}$$

where // represents a parallel combination of inductances. The currents I_1 and I_2 can therefore be adjusted to compensate for the mechanical asymmetry, and the ratio I_2/I_1 thus obtained measures the original asymmetry before it was balanced. We shall determine the ratios on both sides of Eq. (6) to check against the theory. This check will also indicate how good a "symmetric component-accelerometer approximation" is. Such an approximation shall often be used later for simplicity.

The parameters measured in a particular cool down are summarized in Table I. The uncoupled mechanical frequencies of the proof masses were measured at 4.2 K with the gradiometer assembly firmly attached to an effectively infinite mass platform. This platform is simply the Dewar and the ground. We have measured ${\omega_{2M}}^2/{\omega_{1M}}^2 = 0.92$, and the mass ratio m_2/m_1 is estimated to be close to unity. Therefore, the ratio of the measured mechanical frequencies reflects the mismatch in the spring constants for the two proof masses.

The experimental values of the various inductances

TABLE I. Experimental parameters of the gravity gradiometer.

Parameter	Symbol	Value
Mass of each proof mass	m_k	0.40 kg
Mass of gradiometer assembly	M	7.7 kg
Mass ratio	m_k/M	0.052
Mechanical proof mass frequency	$\bar{f}_{kM}$	19 Hz
Mechanical spring constant ratio	${\omega_{2M}}^2/{\omega_{1M}}^2$	0.92
Gradiometer base line	l	0.16 m
Pancake coil area	A_L	2019 mm^2
Pancake coil wire density	n_L	11 mm^{-1}
Inductance per spacing	$\Lambda \equiv \mu_0 {n_L}^2 A_L$	0.306 H m^{-1}
Coil-to-proof-mass spacing	$\bar{d}_L$	0.14 mm
Inductance of one coil	$\bar{L}$	42 μH
Measured coil spacing asymmetries	$\frac{L_{1b}-L_{1a}}{L_{1b}+L_{1a}}$	0.15
	$\frac{L_{2b}-L_{2a}}{L_{2b}+L_{2a}}$	0.34
Sensing loop asymmetry	$\frac{L_{2b}//L_{2a}}{L_{1b}//L_{1a}}$	0.91
Geometric asymmetry factor	$\frac{L_{2b}//L_{2a}}{L_{1b}//L_{1a}}\frac{{\omega_{2M}}^2}{{\omega_{1M}}^2}$	0.83

shown in the circuit diagram of Fig. 3 can be measured only when the system becomes superconducting. The method of stored flux measurement described in Sec. II B was employed to measure various loop inductances. The measured series inductances $L_{1b}+L_{1a}$ and $L_{2b}+L_{2a}$ agree with the inductances calculated from Eq. (2).

In order to measure the individual inductances or the parallel inductance $L_{ka}//L_{kb}$, we used an *acceleration-response method* to measure the ratios L_{1b}/L_{1a} and L_{2b}/L_{2a}. This method does not require knowledge of the behavior of L_0. A very small stored current is used so that negligible shifts are produced in the equilibrium position of the proof mass and in the proof mass resonance frequency. When a current is stored on only one side, say on side one, the accelerometer sensitivity is proportional to the effective current:

$$I_1'=I_1+\frac{L_{1b}-L_{1a}}{L_{1b}+L_{1a}}i_1=\frac{L_{1b}I_{1a}-L_{1a}I_{1b}}{L_{1b}+L_{1a}}\ , \tag{7}$$

as can be seen from Eqs. (34) and (46a) of paper I. The accelerometer sensitivity is first measured with $I_{1a}=I_t$, $I_{1b}=0$; and is then remeasured with $I_{1a}=0$, $I_{1b}=I_t$. The ratio of these two sensitivities is L_{1b}/L_{1a} by Eq. (7). The asymmetry factors $(L_{1b}-L_{1a})/(L_{1b}+L_{1a})$ and $(L_{2b}-L_{2a})/(L_{2b}+L_{2a})$ are then found to be 0.15 and 0.34, respectively, and the ratio of $L_{2b}//L_{2a}$ to $L_{1b}//L_{1a}$ is 0.91. The geometric asymmetry factor can now be calculated as

$$\frac{L_{2b}//L_{2a}}{L_{1b}//L_{1a}}\frac{\omega_{2M}{}^2}{\omega_{1M}{}^2}=0.83\ .$$

The supercurrent ratio, $-I_2/I_1$, required to compensate for this asymmetry is found to be 0.84, so that the two measurements are in agreement within the errors.

B. Accelerometer mode and gradiometer mode

In the *gradiometer mode,* the supercurrents are stored such that only differential accelerations at the two component accelerometers will produce signals. A common acceleration is "current-differenced" out before detection. If the relative polarity between the supercurrents at the two component accelerometers are reversed, the differential acceleration signals will then be current-differenced out. The gradiometer is, thus, activated in a *"common accelerometer mode."* Being an identical electromechanical system, the accelerometer mode has the same characteristics toward common accelerations as the gradiometer mode has toward differential accelerations.

In the experiment, the application of a pure acceleration is much easier than that of an acceleration gradient. Interchangeability of the roles between common and differential accelerations therefore provides us with an alternate method to evaluate and calibrate the gradiometer. This method is highly sensitive because a known acceleration can be applied with a much higher amplitude than a gravity gradient.

In each mode of *circuit operation,* the two coupled component accelerometers have 2 degrees of freedom and will have two normal modes of *motion.* The two proof masses move with the same phase in one mode at a frequency ω_+ and with opposite phases in the other mode at a frequency ω_-. These normal mode frequencies and Q's can be measured experimentally and provide information on the gradiometer parameters. We will first show how they are related to the gradiometer parameters.

The equations of motion and their constraints have been given in Eqs. (41) and (42) of paper I. Strictly speaking, the normal mode frequencies ω_+ and ω_- are obtained as eigenfrequencies of these equations. This can be done by first eliminating the current coordinates $i_d(\omega)$ and $i_c(\omega)$. For free oscillations, i.e., when $g_d(\omega)=g_c(\omega)=0$, the dynamical equations become

$$(-\omega^2+\omega_{1M}{}^2)\left[\frac{(L_0+L_{1p})m_1}{\Lambda^2 I_1'{}^2}+1\right]x_1 +(-\omega^2+\omega_{2M}{}^2)\frac{L_0 m_2}{\Lambda^2 I_1' I_2'}x_2=0\ , \tag{8a}$$

$$(-\omega^2+\omega_{1M}{}^2)\frac{L_0 m_1}{\Lambda^2 I_1' I_2'}x_1 +(-\omega^2+\omega_{2M}{}^2)\left[\frac{(L_0+L_{2p})m_2}{\Lambda^2 I_2'{}^2}+1\right]x_2=0\ , \tag{8b}$$

where the frequency dependence of x_1 and x_2 have been omitted for simplicity. The resulting eigenfrequencies are given in Ref. 10. We shall obtain approximate solutions in simpler forms to illustrate the physics.

The two component accelerometers in our gradiometer are partially matched geometrically. We use the *symmetric component-accelerometer approximation:*

$$m_1=m_2\ , \tag{9a}$$

$$\omega_{1M}=\omega_{2M}\ , \tag{9b}$$

$$L_{1s}=L_{2s}\ , \tag{10a}$$

$$L_{1p}=L_{2p}\ . \tag{10b}$$

In this case, a wideband balance could be achieved without introducing i_1 and i_2. If we now take $I_1=-I_2$ in the gradiometer mode, the eigenfrequencies are just given by

$$\omega_+=\omega_{1c}=\omega_{2c}\ , \tag{11a}$$

$$\omega_-=\omega_{1d}=\omega_{2d}\ , \tag{11b}$$

to the leading term in the above approximation. In the accelerometer mode in which $I_1=I_2$, the frequencies are reversed:

$$\omega_+=\omega_{1d}=\omega_{2d}\ , \tag{12a}$$

$$\omega_-=\omega_{1c}=\omega_{2c}\ . \tag{12b}$$

The frequencies ω_{kc} and ω_{kd} are effective frequencies for the "complementary" current (i_c) and "additive" current (i_d) modes, as is evidenced from their definitions in Eq. (43) of paper I, and are *theoretical* parameters for describing the operation of the gradiometer. The normal mode frequencies of motion, ω_+ and ω_-, on the other hand, are *physically measurable* quantities that provide us with approximate values of ω_{kc} and ω_{kd}.

When the gradiometer assembly is suspended by a weak spring system of a low resonance frequency Ω, the gradiometer platform has a finite mass M and will couple with the pair of masses. The three frequencies, Ω, ω_+, and ω_-, will all be shifted, and the equations of motion are modified. If we denote the platform position by X and measure the proof mass coordinates relative to it, the kinetic energy of the system is

$$T=\tfrac{1}{2}[M\dot{X}^2+m_1(\dot{X}+\dot{x}_1)^2+m_2(\dot{X}+\dot{x}_2)^2]\ , \tag{13}$$

and the potential energy V has an additional term $\frac{1}{2}M\Omega^2X^2$. The linearized equations of motion, Eq. (37) of paper I, are then modified into

$$-\omega^2[(M+m_1+m_2)X+m_1x_1+m_2x_2]+M\Omega^2X=0\ , \tag{14a}$$

$$-\omega^2m_1(X+x_1)+m_1\left[\omega_{1M}{}^2+\frac{\Lambda^2i_1{}^2}{m_1L_{1s}}\right]x_1 +\Lambda I_1'i_1(\omega)=0\ . \tag{14b}$$

$$-\omega^2m_2(X+x_2)+m_2\left[\omega_{2M}{}^2+\frac{\Lambda^2i_2{}^2}{m_2L_{2s}}\right]x_2 -\Lambda I_2'i_2(\omega)=0\ . \tag{14c}$$

These equations are subject to the constraints given by Eq. (38) of paper I.

We again make the approximation of Eqs. (9) and (10), along with $i_1=i_2=0$. In the gradiometer mode ($I_1=-I_2$), the eigenfrequency of the "out-of-phase mode" ($x_1=-x_2$) of motion is unchanged:

$$\omega_{G-}{}^2=\omega_{kd}{}^2\ ; \tag{15a}$$

whereas, the "in-phase mode" ($x_1=x_2$) eigenfrequency is shifted to

$$\omega_{G+}{}^2=\left[1+\frac{2m_k}{M}\right]\omega_{kc}{}^2\ . \tag{15b}$$

Here we have made an approximation based on $\omega_{kM}{}^2\gg\Omega^2$. In the accelerometer mode ($I_1=I_2$), we find

$$\omega_{A-}{}^2=\omega_{kc}{}^2\ , \tag{16a}$$

$$\omega_{A+}{}^2=\left[1+\frac{2m_k}{M}\right]\omega_{kd}{}^2\ . \tag{16b}$$

The parameters $\omega_{kc}{}^2$ and $\omega_{kd}{}^2$ are functions of $I_k{}^2$:

$$\omega_{kc}{}^2=\omega_{kM}{}^2+\frac{\Lambda^2I_k{}^2}{m_kL_{kp}}\ , \tag{17a}$$

$$\omega_{kd}{}^2=\omega_{kM}{}^2+\frac{\Lambda^2I_k{}^2}{m_k(L_{kp}+2L_0)}\ , \tag{17b}$$

as obtained from Eqs. (44) of paper I.

The shifted frequencies, f_{G-}, f_{G+}, f_{A-}, and f_{A+}, measured as functions of I_k are presented in Fig. 5. The intercepts to $I_k{}^2=0$ are given by

$$f_{G-}{}^2(0)=f_{A-}{}^2(0)=f_{kM}{}^2\ , \tag{18a}$$

$$f_{G+}{}^2(0)=f_{A+}{}^2(0)=\left[1+\frac{2m_k}{M}\right]f_{kM}{}^2\ , \tag{18b}$$

Taking the ratio of the two intercepts enables a measurement of the mass ratio. We obtain $m_k/M=0.052\pm0.006$, which is in agreement with the value given in Table I.

The slopes of the graphs for $\omega_{A-}{}^2$, $\omega_{A+}{}^2$, $\omega_{G-}{}^2$, $\omega_{G+}{}^2$ versus $I_k{}^2$ are

$$\frac{\Lambda^2}{m_kL_p},\quad\left[1+\frac{2m_k}{M}\right]\frac{\Lambda^2}{m_k(L_{kp}+2L_0)},\quad \frac{\Lambda^2}{m_k(L_{kp}+2L_0)},\quad\left[1+\frac{2m_k}{M}\right]\frac{\Lambda^2}{m_kL_{kp}}\ , \tag{19}$$

respectively. From these, we obtain an inductance ratio:

$$\frac{2L_0}{L_{kp}}=1.58\pm0.14\ . \tag{20}$$

This result indicates that the output impedance has been chosen sufficiently large. Using the value of $\Lambda=0.306$ $\mathrm{H\,m^{-1}}$ calculated from Eq. (15) of paper I, we find $L_{kp}=23\ \mu$H, which is consistent with inductance values in Table I. Also, we obtain $L_0=18\ \mu$H. Consistency in the measurements indicate that the symmetric component accelerometer approximation is sufficiently good for diagnostic purposes.

The output inductance L_0 is the equivalent inductance at the transformer primary when the secondary is loaded by the SQUID input of approximately 2 μH. The transformer has a turns ratio of 69:19 with calculated inductances of 42 and 3.2 μH, respectively, to a 20% accuracy. L_0 can then be calculated from Eq. (75) of paper I, and would have the above measured value of 18 μH if we take the transformer coupling factor to be $k_t{}^2=0.93$. However, the power transfer function of the transformer would then only be $H_p^{\mathrm{I,II}}=0.51\pm0.10$, as one can see from Eq. (76) of paper I. The transformer has not been optimized in the past assembly, but this is not a problem until one reaches the amplifier-limited sensitivity. The resulting value of the effective electrical energy coupling to the SQUID is $\eta=0.31$.

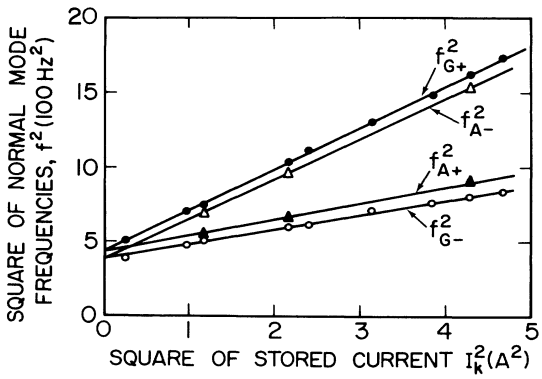

FIG. 5. Normal mode frequencies of the gradiometer as functions of the stored current.

C. Circuit optimization and transfer functions

Equation (53) of paper I shows that the gradiometer transfer function, $H_{gi}^{d}(\omega)$, of an equivalent accelerometer is proportional to I'/ω_0^2 in the low signal-frequency limit. In the symmetric component-accelerometer mode, ω_0 is identified with ω_{kd}.

In Fig. 6 we plot a measured curve of $|I_k|/f_0^2$ versus $|I_k|$ to indicate the functional dependence of the differential-acceleration-to-response-current transfer function on the stored current $|I_k|$. This plot shows that the gradiometer sensitivity first increases as $|I_k|$ is increased from 0, and then slows down due to an increase in f_0 caused by an increasing $|I_k|$. The gradiometer is expected to reach its maximum sensitivity when $f_0^2 \simeq 2f_{kM}^2$ at $|I_k| \simeq 2$ A. However, this maximum is very smooth so that a smaller current can be used without a substantial reduction in sensitivity.

If the gradiometer sensitivity is SQUID noise limited, optimizing the above transfer function yields a maximum signal-to-noise ratio for the gradiometer. However, if the sensitivity is limited by the Brownian motion noise, one would have to maximize the function $Q_-^{1/2}|I_k|/f_0^2$ instead, where Q_- is the quality factor of the out-of-phase mode: $f_{G_-}=f_0$.

In Sec. III of paper I, we used the response current in L_0 to define transfer functions in harmony with the model of a reduced equivalent accelerometer. Here we prefer using the response current *at the SQUID input* L_i, a quantity which can be directly calibrated using the SQUID transfer function.

The in-phase mode of motion has the parameters

$$m_+ = 2m_k \ , \tag{21}$$

$$x_+ = \frac{x_2+x_1}{2} \ . \tag{22}$$

In the calibration experiment, a common acceleration is provided by applying a sinusoidal displacement $X(\omega)$ to the gradiometer assembly. In this case, Eqs. (14) can be solved to obtain

$$(-\omega^2+\omega_0^2)x_+(\omega)=\omega^2 X(\omega)\equiv g_c(\omega) \ . \tag{23}$$

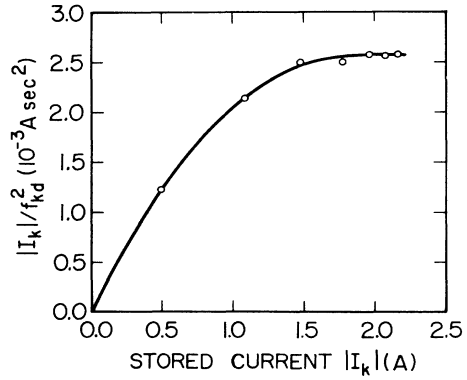

FIG. 6. Sensitivity scaling of the gradiometer as a function of the stored current.

This acceleration produces a response current $i_+(\omega)$ which is proportional to $x_2+x_1=2x_+$. The displacement-to-current transfer function is

$$H_{xi}^{A}(\omega)=\frac{i_+(\omega)}{x_+(\omega)}=\frac{2i_+}{(x_2+x_1)_+} \ . \tag{24}$$

At a low frequency $\omega \ll \omega_0$, the *acceleration-to-current transfer function* is

$$H_{gi}^{A}(\omega)=\frac{i_+(\omega)}{g_c(\omega)}=\frac{2}{\omega_0^2}\frac{i_+}{(x_2+x_1)_+} \ . \tag{25}$$

The parameters for the out-of-phase motion are

$$m_- = \frac{m_k}{2} \ , \tag{26}$$

$$x_- = x_2 - x_1 \ . \tag{27}$$

Notice that m_- is the *effective mass* m of the gradiometer defined in Sec. III E of paper I. In the gradiometer mode, a differential acceleration $g_d(\omega)$ produces a differential proof mass displacement x_- with

$$(-\omega^2+\omega_0^2)x_-(\omega)=g_d(\omega) \ . \tag{28}$$

The response current $i_-(\omega)$ is proportional to just $x_2-x_1=x_-$. The displacement-to-current transfer function is therefore

$$H_{xi}^{G}(\omega)=\frac{i_-(\omega)}{x_-(\omega)}=\frac{i}{(x_2-x_1)_-} \ . \tag{29}$$

The *gravity-gradient-to-current transfer function* for $\omega \ll \omega_0$ is

$$H_{\Gamma i}^{G}(\omega)=\frac{i_-(\omega)}{\Gamma(\omega)}=\frac{l}{\omega_0^2}\frac{i_-}{(x_2-x_1)_-} \ , \tag{30}$$

where l is the base line and $\Gamma(\omega)\equiv g_d(\omega)/l$.

If the same magnitudes of stored currents are used in the two modes of circuit operation, the following equality is obeyed by the two equivalent circuits:

$$\frac{i_-}{(x_2-x_1)_-}=\frac{i_+}{(x_2+x_1)_+} \ . \tag{31}$$

The transfer functions in the two circuit modes are therefore related by

$$H_{\Gamma i}^{G}(\omega)=\frac{l}{2}H_{gi}^{A}(\omega) \ . \tag{32}$$

This simple relationship follows because Eq. (25) and (30) contain the same resonance frequency ω_0, as is expected from Eqs. (11b) and (12a).

The function $H_{gi}^{A}(\omega)$ is measured by applying a sinusoidal acceleration $g_c(\omega)=\omega^2 X(\omega)$ to the gradiometer assembly at ω below 1 Hz. The response current is measured with the SQUID amplifier which has a current-to-voltage transfer function of 0.20 V μA^{-1}. The acceleration is applied to the gradiometer in the vibration isolation system described in Sec. III C. An electromagnetic shaker is coupled with a weak latex tubing from one side to the other of a vibration isolation stage (see Fig. 4) to provide a vertical acceleration to the gradiometer. The

weak tubing acts as an attenuator, permitting a good signal-to-noise ratio without degrading the vibration isolation. The platform acceleration produced by the shaker has been calibrated by measuring its displacement and later confirmed with a commercial accelerometer.

Figure 7 shows the calibration of the accelerometer mode measured in terms of the current response i_+ at the SQUID input as a function of the applied acceleration g_c. Very small stored currents are used because of the extremely high sensitivity of the accelerometer. From the graph we obtain a transfer function of (1.55 ± 0.05) mA per m sec^{-2} for the accelerometer with only $I_k=1$ mA stored on each side. The transfer function should be linear with the stored currents for low current values that produce negligible shifts of proof mass frequencies. This linearity is confirmed by Fig. 8, which is a plot of the measured acceleration-to-current transfer function as a function of I_k.

At high currents, the calibration curve in Fig. 6, which takes into account frequency shifts, is used to extrapolate our transfer function measurements. We then obtain

$$H_{gi}^{A}(\omega)=\frac{i_+(\omega)}{g_c(\omega)}=(1.6\pm0.1)\ \mathrm{A(m\,sec^{-2})^{-1}} \qquad (25')$$

for a near optimum current value of $I_k=1.5$ A. Converting this value to the transfer function in the gradiometer mode, we have

$$H_{\Gamma i}^{G}(\omega)=\frac{i_-(\omega)}{\Gamma(\omega)}=\frac{0.16\,\mathrm{m}}{2}\,\frac{1.6\,\mathrm{A}}{1\,\mathrm{m\,sec^{-2}}}$$

$$=(0.13\pm0.01)\ \mathrm{nA\,E^{-1}}\ . \qquad (32')$$

The SQUID amplifier noise, when loaded with the fully charged gradiometer, was measured to be $S_i^{1/2}(f)=8.9$ pA Hz$^{-1/2}$, which corresponds to $E_A(f)=7.9\times10^{-29}$ J Hz$^{-1/2}$ for $L_i=2$ μH, at a high frequency (>60 Hz) where the proof mass displacement noise becomes negligible. This noise level would correspond to an amplifier-limited gravity gradient noise of 0.069 E Hz$^{-1/2}$. This

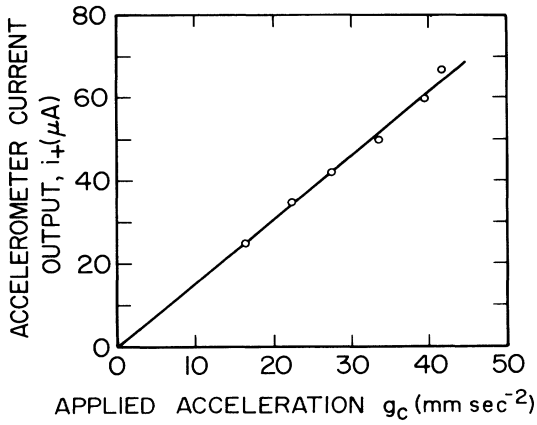

FIG. 7. Calibration in the accelerometer mode with 1-mA stored currents.

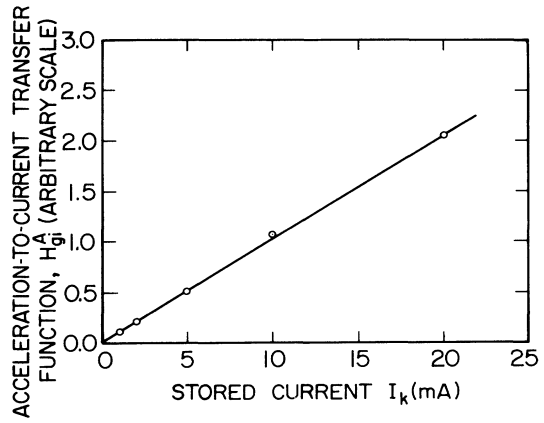

FIG. 8. Sensitivity scaling in the accelerometer mode as a function of the stored current.

value is in close agreement with the theoretical sensitivity of 0.068 E Hz$^{-1/2}$ which is obtained by directly substituting the measured SQUID noise and the measured values of $\eta=-0.31$ and $\beta=0.53$ into Eq. (79) of paper I. In our tests the gradiometer noise at low frequencies was limited by seismic noise at 0.3—0.7 E Hz$^{-1/2}$ level. Therefore, we would not lose sensitivity by using a somewhat smaller gain. Stored currents of 0.55 A were used in the tests reported in Sec. VI. The transfer function deduced from the accelerometer mode calibration gives 62 pA E^{-1} at this current level. In Sec. VI A, we will check this value with the direct calibration of the gradiometer which employs gravity gradient signals.

V. INVESTIGATION OF INSTRUMENT NOISE AND ERRORS

A. Environmental noise and common mode balance

Vibrations were found to be the most serious environmental noise. Our early tests with the gradiometer rigidly mounted inside a liquid N_2 shielded He Dewar have encountered a vibration noise energy of 10^{-8} J at the proof mass resonance frequency of 19 Hz. Such a noise level corresponds to an equivalent Brownian motion at a noise temperature of 7×10^{14} K, which is 10^7 times the 4-K Brownian motion in vibration amplitude.

When the gradiometer is balanced against common accelerations, its response to the vibration noise is greatly reduced. In the experiment, however, the gradiometer can be balanced only if we can use its acceleration response as a guide. Sufficient vibration isolation to achieve a noise level of the unbalanced gradiometer well within the amplifier dynamic range is therefore essential. A minimum of 60 dB isolation is required at the proof mass resonance frequencies in order to be able to operate at the full sensitivity of the accelerometers.

If vibrations have a white acceleration spectrum, the low-frequency noise will be Q times less than that at the proof mass resonances; thus, this noise will not overload the amplifier. Therefore, we chose to start with vibration isolation at higher frequencies where the SQUID ampli-

fier was being overloaded. This isolation would enable us to balance the accelerations and obtain a working gradiometer.

If the proof mass acceleration noise amplitude can be reduced by 4 orders of magnitude, one will be able to observe the actual Brownian motion at the resonances in a gradiometer with a 60-dB balance. Although such an observation may not improve the acceleration noise at the low-frequency end, it could prove to be very informative. This observation would determine the Brownian motion level of the instrument, and show whether the observed acceleration noise comes from the environment or from the intrinsic noise of the instrument.

Although an electronic "cold damping" technique[8,10] could have been applied to selectively filter the vibration noise at the proof mass resonances, there were other modes in the environment which require wideband isolation. Therefore, we chose to develop a passive vibration isolation system with which the gradiometer can be tested in its simplest form. Satisfactory vibration isolation of the gradiometer was an essential step in leading to a successful demonstration of its performance and the operation of the device as a detector in the inverse-square law experiment.[7,5] Various combinations of low-pass vibration filters were tried to isolate the noise coming from the ground and the Dewar. Filters were improved in steps with the guidance of vibration data obtained in each step.

With the three-stage vibration isolation system described in Sec. III C, the noise at the proof mass resonance decreased to 2×10^{4} K, corresponding to a displacement of 5×10^{-12} m. The achieved improvement at 20 Hz was therefore better than 100 dB. At frequencies above 60 Hz, the spectrum indicated the SQUID-limited noise level.

We now turn to the wideband common mode balance method described in Sec. III D of paper I. In this method, calibrated sinusoidal acceleration signals are provided in the vertical direction by means of an electromagnetic shaker. Two out of the three stored currents I_1, I_2, and i_2 are iteratively adjusted for balance at 0.9 Hz ($\ll\omega_0/2\pi$) and 70 Hz ($\gg\omega_0/2\pi$) in turn. This is a painstaking procedure since a balance point is searched for in a two-dimensional parameter space and sufficient time should be allowed after each adjustment of currents for the mechanical disturbance of the system to damp down.

Figure 9(a) shows the 0—50-Hz noise spectrum of the gradiometer balanced in the wideband to 1 part in 10^3. The transfer functions are obtained from the accelerometer mode calibrations using the relationships discussed in Sec. IV. This procedure gives

$$[H_{gi}^{G}(\omega)]^{-1}=\omega_0^2 x_-/i_-=1.29\ \text{m sec}^{-2}\,\text{A}^{-1}\ .$$

The gradiometer is less sensitive to external common accelerations now. Shown in the spectrum is the differential mode of the masses at $f_0=\omega_0/2\pi=24.8$ Hz of an rms amplitude $\omega_0^2 x_-=2.75$ nm sec^{-2}. The noise temperature for this mode is given by

$$\frac{1}{k_B}\left[\frac{m_k}{2}\right]\omega_0^2 x_-^{\,2}=4.5\ \text{K}\ . \tag{33}$$

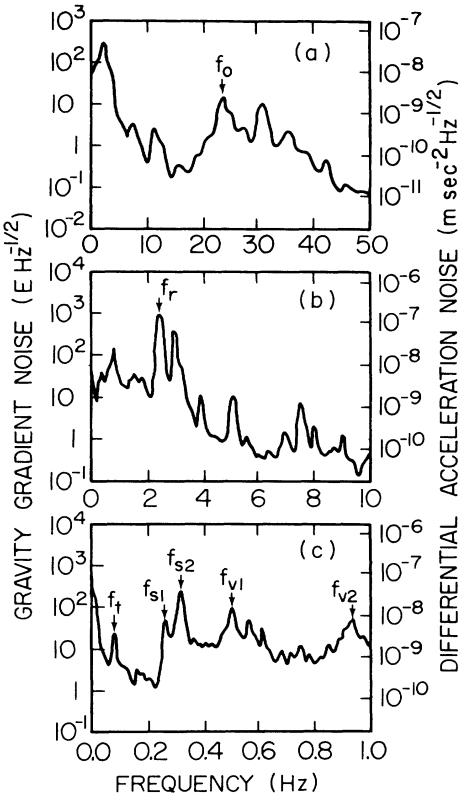

FIG. 9. Noise spectrum of the gradiometer on a three-stage vibration isolation system.

Thus, this spectrum represents the *observation of the Brownian motion* of the proof masses in the differential mode at the liquid-He temperature. All other peaks are attenuated by about 10^3, which is the degree of balance obtained. These data confirm that the observed noise is almost entirely environmental and is not intrinsic to the gradiometer.

Figure 9(b) shows the 0—10-Hz spectrum. The vertical scale of the plot has been calibrated by using the accelerometer mode, and confirmed by a direct calibration with a known gravity gradient signal which will be explained in Sec. VI. The noise in the 5—10-Hz band reaches below 1 E Hz$^{-1/2}$ but the background seems to be close to 0.3 E Hz$^{-1/2}$. Excessive vibration noise has degraded the spectrum at several peaks. The noise in the 1—4-Hz range is heavily contaminated by the rocking mode of the gradiometer (f_r) at 2.5 Hz and other modes associated with the vibration isolation system. The 0—1 Hz spectrum shown in Fig. 9(c) exhibits the swinging modes (f_{s1},f_{s2}) around 0.3 Hz, the vertical Dewar suspension mode (f_{v1}) at 0.5 Hz, the vertical gradiometer rubber suspension mode (f_{v2}) at 0.9 Hz, and a torsional mode (f_t) at 0.08 Hz.

Our low-pass filters introduced numerous peaks at their own resonances. These filters were needed initially to prevent the SQUID from overloading at the higher-frequency peaks. After the common mode balance, the gradiometer became intrinsically insensitive to the environmental noise. Therefore, in the gradiometer mode, the

filters could be reduced to a minimum. We found a single-stage filter provided by the rubber tubing inside the vacuum was sufficient for a balanced gradiometer and eliminated many undesirable peaks from the signal bandwidth.

B. Gradiometer noise

Figure 10 shows the noise spectra of the gradiometer obtained with the single-stage filter. The upper trace is the noise spectrum measured with the gradiometer in the accelerometer mode. The lower trace is the gradiometer output after the common mode balance to 3 parts in 10^5 has been achieved toward an applied acceleration at 0.18 Hz. The SQUID noise limit of 0.069 E Hz$^{-1/2}$ with the associated $1/f$ noise is plotted by a dotted line. The vertical scale shows both the acceleration and gradient noise calibrations, which are related by Eq. (32). The ratio of the two spectra at any frequency, therefore, represents the actual reduction of noise outputs at that particular frequency as a result of the balance.

First, comments are due for the measured acceleration noise spectrum (top trace). The general structure of this spectrum, which contains a broad peak around 0.25 Hz and a dip around 0.1 Hz, and the noise level of approximately 2.5×10^{-7} m sec^{-2} Hz$^{-1/2}$ at 0.5 Hz are obtained consistently from run to run after waiting sufficiently long for resonances in the gradiometer platform to damp down. This noise data has been reproduced by using conventional accelerometers mounted at the room temperature end of the pendulum suspension and on the laboratory floor, with the exception of the dip at 0.1 Hz for which the room-temperature accelerometers did not have enough resolution. Since the data represents the residual acceleration noise of a deep-underground laboratory, the upper curve in Fig. 10 must reflect *geophysically significant* seismic activity, except for the broad peak near 1 Hz which is due to the low-Q vertical mode of the rubber suspension. It is noteworthy that, while acceleration noise

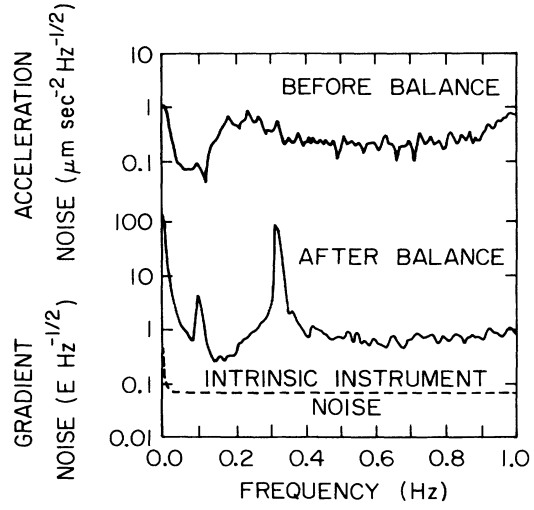

FIG. 10. Low-frequency noise spectra of the gradiometer on a single-stage vibration filter.

spectra measured at the top end of the pendulum in the vertical and horizontal directions looked similar, the noise output of the superconducting accelerometer correlated closely ($>90\%$) with the vertical acceleration. This correlation indicates that the horizontal acceleration is indeed attenuated by the pendulum action, as has been predicted by the analysis shown in Appendix A. Since the gradiometer is pointing at an umbrella angle $\theta_u=\arctan\sqrt{2}=54.7°$, the noise spectrum of Fig. 10 should then be raised by a factor of $\sec\theta_u=\sqrt{3}$ to obtain the proper calibration of the vertical acceleration noise at College Park, Maryland.

The lower trace of Fig. 10 represents a *typical* residual noise spectrum of a balanced gradiometer, with the exception of the 0.1-Hz peak of the torsional mode which disappears into the background noise in the quietest situations. Unlike the torsional mode, however, the swinging mode at 0.32 Hz is always present with its peak at around 100 E Hz$^{-1/2}$ level. Also persistently present is the low-frequency excess noise below 0.1 Hz. The noise level is approximately 0.7 E Hz$^{-1/2}$ between 0.5 and 0.9 Hz and reaches a minimum value of 0.3 E Hz$^{-1/2}$ in a narrow window around 0.15 Hz. Comparison of the two traces reveals that the noise was reduced only by a factor of 3×10^3, which represents a discrepancy of a factor of 10 from the value expected from the common mode balance. Another noticeable feature is that, although the general structure of the background spectrum of the balanced gradiometer, with the resonance peaks removed, appears similar to the shape of the acceleration noise, the two spectra are not well correlated. Therefore, the residual noise of the gradiometer must be coming from a source other than vertical acceleration.

It is desirable to determine the Brownian motion noise level of the instrument. The power spectral density of the thermal noise of the gradiometer is given in Eq. (87) of paper I:

$$S_{\Gamma,B}(f)=\frac{8}{m_1 l^2}\frac{k_B T}{\tau(f)}\ . \tag{34}$$

It is difficult to measure the effective damping time $\tau(f)$ at $f\ll f_0$ directly. If one assumes the "white acceleration noise model," $\tau(f)$ in Eq. (34) can be replaced by the measured quantity $\tau(f_0)$. The measured Q values are of the order of 5×10^4 and are probably pressure limited. This implies $\tau(f)=3.2\times10^2$ sec and $S_{\Gamma,B}{}^{1/2}(f)=0.01$ E Hz$^{-1/2}$ for our gradiometer. If, on the other hand, the effective Q is assumed to be independent of frequency, the Brownian motion noise would become frequency dependent:

$$S_{\Gamma,B}{}^{1/2}(f)=0.01\ \text{E Hz}^{-1/2}\left[\frac{f}{f_0}\right]^{1/2}\ . \tag{35}$$

In either case, the thermal noise would be negligible compared to the SQUID noise level of 0.069 E Hz$^{-1/2}$.

We therefore conclude that the observed noise spectrum is *extrinsic* to the instrument and is due to error mechanisms which couple environmental noise into the gradiometer output. Error sources responsible for the ob-

served residual noise of the gradiometer are identified in the following section with the aid of the appendixes.

C. Instrument errors

The dynamics of a platform suspended as a pendulum is analyzed in Appendix A. The pendulum decouples the gradiometer from angular motions of the external world. The horizontal acceleration transmitted to the gradiometer is almost exactly canceled by the modulated Earth's gravity which is caused by the induced tilt of the instrument. It is found, however, that the resulting angular velocity and angular acceleration can couple to the gradiometer through centrifugal acceleration and through the misalignment of the effective gradiometer sensitive axis with respect to the base line. Since the vertical component of linear acceleration is balanced out to a sufficient degree, the horizontal acceleration can produce a limiting instrument error by driving a *secondary* angular motion.

Experimentally, the noise of the unbalanced gradiometer correlates with the external acceleration in the vertical direction. This correlation and the absence of a pronounced resonance peak at the pendulum frequency $f_p = 0.32$ Hz in the upper trace of Fig. 10 prove that the horizontal vibration isolation by the pendulum action really works for an *accelerometer.* A close examination of the noise spectrum reveals a *barely visible* resonance peak at f_p above the background noise. This result renders a remarkable proof for the theory developed in Appendix A. According to Eqs. (A13), the horizontal acceleration sensed by an accelerometer under the pendulum suspension should be peaked at its resonance with a net gain of unity. Since the measured frequency spectra of the horizontal and vertical accelerations agree within 10 dB, the superconducting accelerometer pointing at an umbrella angle should measure a horizontal acceleration with a maximum amplitude of approximately three times that of the vertical acceleration at f_p. Therefore, the horizontal acceleration peak sticks out barely above the vertical acceleration background.

The analysis in Appendix A also leads to a prediction that, for a *gradiometer,* the overall effect of the pendulum action is that of a wideband attenuator for a horizontal acceleration, with its attenuation improving as the frequency approaches dc. In particular, when $\omega > \Omega_E / |\delta\hat{\mathbf{n}}_{+\hat{l}}|$, the dominant coupling mechanism for the horizontal acceleration is the induced angular acceleration, as given by Eq. (24). Below this frequency, the centrifugal acceleration error dominates. The crossover frequency is 10^{-2} Hz when $|\delta\hat{\mathbf{n}}_{+\hat{l}}| = 10^{-3}$. The frequency response of the angular acceleration, $|h_\alpha(\omega)|$, has been plotted in Fig. 11. One can see a strong resemblance between this curve and the gradiometer output, the bottom trace of in Fig. 10, above 0.2 Hz. In fact, the agreement improves when the spectrum of the driving background acceleration is taken into account. In Fig. 12 we plot typical observed spectra for the vertical (top dotted line) and horizontal (top dashed line) accelerations $\mathbf{A}_z(\omega)$ and $\mathbf{A}_h(\omega)$ as well as the gradiometer noise output (solid line). The residual vertical acceleration expected from the vertical common mode balance of 90 dB is plotted by the bottom dotted line. The bottom dashed line is a fit obtained by multiplying the spectrum for $\mathbf{A}_h(\omega)$ with its transfer function through the angular acceleration. The misalignment error required for this fit is $|\delta\hat{\mathbf{n}}_{+\hat{l}}| \simeq 7\times10^{-4}$, which is in close agreement with the value determined from the observed centrifugal acceleration: $|\delta\hat{\mathbf{n}}_{+\hat{l}}| = 6\times10^{-4}$ (see Appendix B). Notice that the gradiometer noise above 0.2 Hz is completely accounted for by this single error mechanism: *the horizontal acceleration coupled through the induced angular acceleration.*

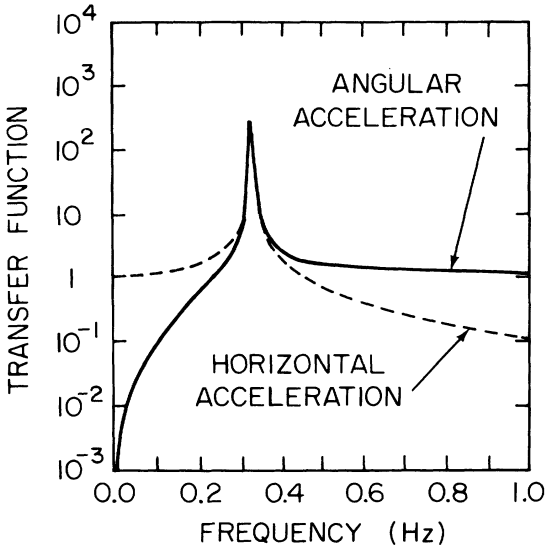

FIG. 11. Transfer functions of the pendulum suspension for horizontal accelerations.

The value of $\delta\hat{\mathbf{n}}_{+\hat{l}}$ (the misalignment of the average

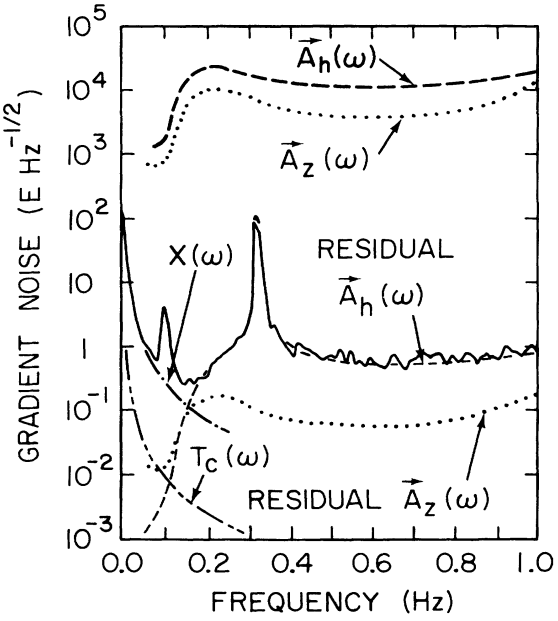

FIG. 12. Various error contributions to the gradiometer noise spectrum.

sensitive axis of the gradiometer with respect to the base line vector $\hat{l}$) found above is rather large in view of the fact that the parallelism of the mating surfaces of the mechanical components of the gradiometer was specified to 5×10^{-5}. This mechanical precision implies that the experimental value of $\delta\hat{\mathbf{n}}_-$ (the relative misalignment between the sensitive axes of the component accelerometers) is of the order of 10^{-4}. A similar value could have been obtained also for $\delta\hat{\mathbf{n}}_{+\hat{l}}$ if the center lines of the two accelerometers had been located within 10^{-2} mm from each other, which is certainly feasible. However, without realizing the seriousness of the induced angular acceleration problem, we had left the centering of the accelerometers to crude positioning by the mounting screws. This must have produced a mismatch of the center lines by approximately 0.1 mm, causing the observed misalignment $|\delta\hat{\mathbf{n}}_{+\hat{l}}|=6\times10^{-4}$.

We now turn our attention to the excess noise below 0.1 Hz, seen in Fig. 10. During the experiment, the SQUID electronics was shielded against rf interference to avoid electronics drift. Although instrument drift can be caused by relaxation of trapped magnetic flux,[13] the observed low-frequency noise did not decrease significantly when the ambient magnetic field was reduced by a factor of 10^3 by adding mu-metal shields. With these electrical sources of low-frequency noise eliminated, we suspect the *temperature drift* and various *nonlinear effects* as the most likely sources for the observed excess noise. As has been discussed in the Appendix of paper I, the superconducting gradiometer can be rather sensitive to temperature noise and nonlinearities in the system can down convert the wideband vibration noise to a gradient noise near dc. These low-frequency error mechanisms are analyzed in detail in Appendix B of this paper. Owing to the limited resolution of the Ge thermometer used to monitor the temperature of the gradiometer assembly, the low-frequency noise spectrum due to temperature fluctuation is computed from an independent measurement of the temperature noise of a liquid-He bath of a different experimental setup[8] with the aid of a model for heat conductivity between the He and the gradiometer. The resulting spectrum is found to be

$$[S_{\Gamma,T}(f)]^{1/2}\simeq1.0\times10^{-2}\ \mathrm{E\,Hz^{-1/2}}\left[\frac{0.1\ \mathrm{Hz}}{f}\right]^2. \tag{36}$$

The scale-factor nonlinearity is computed from the second-order circuit equations for component accelerometers, generalized from Eqs. (29) and (33) of paper I. The low-frequency noise expected from this is of comparable magnitude as the temperature effect at 0.1 Hz, but has a slightly different frequency dependence:

$$[S_{\Gamma,cc}(f)]^{1/2}\lesssim1\times10^{-2}\ \mathrm{E\,Hz^{-1/2}}\left[\frac{0.1\ \mathrm{Hz}}{f}\right]^{3/2}. \tag{37}$$

The effect of the centrifugal acceleration is found to be about 2 orders of magnitude smaller than this value.

The temperature noise of Eq. (36) is plotted in Fig. 12 by a dash-dot-dot line. The actual low-frequency noise, denoted by $X(\omega)$, is about 30 times larger than this calculation. Since the temperature drift of the He bath depends on the exact geometry and thermodynamics of the particular cryostat involved, and on account of additional uncertainties in the thermal model of the instrument, the discrepancy by a factor of 30 does not exclude a possibility that the observed low-frequency noise is due to temperature fluctuations. However, because a comparable level of noise is also predicted from the nonlinearity of the instrument, we cannot be conclusive, without further experimental investigations, as to the origin of the observed excess noise below 0.1 Hz. In future experiments, the temperature of the He bath will be regulated, and the gradiometer will be linearized by means of a force rebalance feedback with a hope to eliminate the low-frequency excess noise.

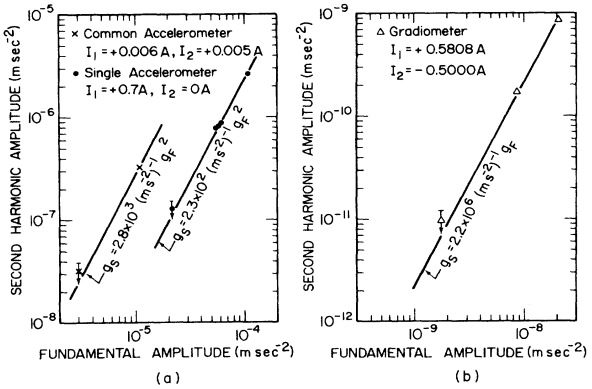

FIG. 13. Second-harmonic generation by the centrifugal acceleration in (a) accelerometer modes and (b) the gradiometer mode.

Another interesting error mechanism discussed in Appendix B is the second-harmonic generation by the centrifugal acceleration. This effect has been observed for large resonance peaks when the system is disturbed mechanically (Fig. 13). During the quiet operation of the instrument, however, no second harmonics were observed above the background noise spectrum of the gradiometer.

VI. GRAVITY GRADIENT MEASUREMENT AND SENSITIVITY CALIBRATION

We shall now describe the gravity gradient calibration with the observation of signals in two types of experiments. A precise calibration of the instrument can be obtained by using a periodic gravity gradient generator and averaging the signal over a number of periods. For such an ac experiment, however, any electrical pickup or mechanical cross coupling at the signal frequency must be eliminated. A "dc" experiment, in which a compact object is brought near the gradiometer and removed, fares better in this regard. Although the use of signal averaging to improve the signal-to-noise ratio is less applicable here, any cross-coupling problem will appear as a transient which can be distinguished from the dc shift in the gradiometer output caused by the gravity signal. We have performed both experiments successfully, as well as an inverse-square law test in which the gradiometer outputs

in three orthogonal orientations of the sensitive axis are summed.

A. ac gravity gradient experiment

The ac calibration of the gradiometer was obtained with a large ($M=1.6\times10^3$ kg) Pb pendulum. The Pb sphere was located approximately in the same horizontal plane with the gradiometer at an average distance r of 2.3 m away. The gradiometer sensitive axis was at an angle of arccot $\sqrt{2}$ with respect to the horizontal plane and was in the plane of swing of the pendulum. The gradiometer thus measured a gravity gradient component given by

$$\Gamma_{11}=-\frac{GM}{r^3}\frac{1}{2}[1+3\cos(2\,\mathrm{arccot}\sqrt{2})]=-\frac{GM}{r^3}\ . \tag{38}$$

When the pendulum swung by $\Delta r(\omega)$, it generated a change in the gravity gradient by

$$\Delta\Gamma_{11}(\omega)=\frac{3GM}{r^4}\Delta r(\omega)\ . \tag{39}$$

The SQUID amplifier output was measured with a spectrum analyzer.

In order to assure that the observed signal was truly gravitational, various precautions were taken. When all three vibration isolation stages were used, excess signals at various harmonics of the pendulum frequency were seen. Correlation studies indicated that a strong second harmonic was generated by an air current driven by the swinging pendulum. This effect was eliminated by shielding the entire apparatus with a wooden enclosure and by using only one rubber filter which was inside the vacuum (see Fig. 4). The possibility of direct mechanical coupling between the pendulum and the gradiometer has also been investigated. With the gradiometer charged in the accelerometer mode and the pendulum swinging at its full amplitude $\pm30°$, we did not see any acceleration signal at the pendulum frequency above the ground noise. The problem of such mechanical coupling has been alleviated by several factors. The pendulum was suspended from the 2-m-thick concrete ceiling; whereas the Dewar sat on a firm floor, 12 m below the ground level, in the basement of the building. Furthermore, the gradiometer was balanced against common accelerations, and the pendulum suspension used for the gradiometer gave isolation of tilt at all frequencies. In order to avoid electrical pickup at the signal frequency, a pneumatic driving mechanism was developed for the Pb pendulum and a natural resonant oscillation was used for most tests.

The rms voltage measured at the pendulum frequency of 0.228 Hz is plotted in Fig. 14 against the calculated rms gravity gradient generated by the pendulum. This plot gives a calibration of 58 pA E^{-1} and agrees with the accelerometer mode calibration, reported in Sec. IV C, to within 7%. This agreement is within our errors. The distance and orientation measurements in either calibration were not intended for high precision.

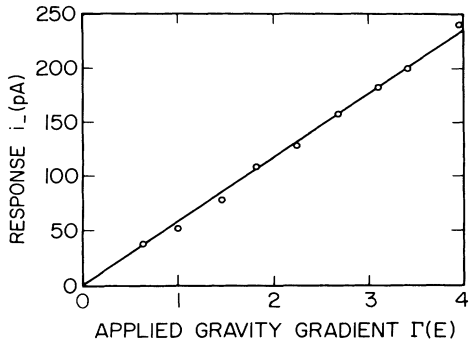

FIG. 14. ac calibration of the gradiometer.

B. dc gravity gradient experiment

The noise spectrum of Fig. 10 indicates that the noise is lower below the 0.3-Hz swinging mode of the platform. In order to perform a dc experiment, we put in active low-pass filters which filtered off the peaks above 0.16 Hz from the amplifier output. The response function of the filters to a step dc voltage change is shown in Fig. 15(a). The characteristic rise time and ripples of the filters will be seen when a step function, gravity gradient signal is applied.

We then moved a Pb brick in and out manually near

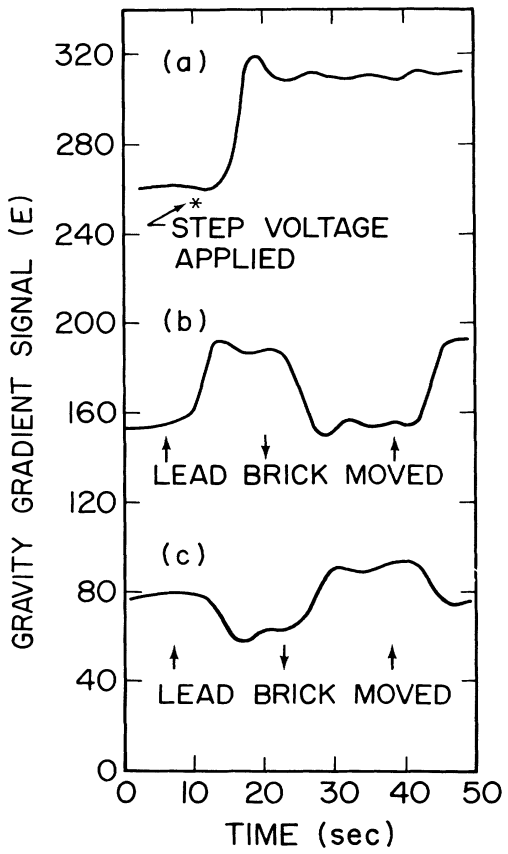

FIG. 15. dc gravity measurements (dc level is arbitrary).

the Dewar at 10—15-sec intervals. The brick weighed 12 kg and was brought to 0.27 m from the gradiometer. The gravity gradient generated was about $GM/r^3 \simeq 40$ E, with a geometrical factor of the order of unity which depends on the exact source-detector orientation.

In Fig. 15(b), the Pb brick was moved in, out, and then in again, roughly in the horizontal plane of the gradiometer. The times and directions of the movement of the Pb brick are indicated by arrows. The line of sight of the source was approximately at an angle of $\operatorname{arccot}\sqrt{2}$ from the gradiometer axis. The expected signal is then

$$\frac{GM}{r^3}\left[1-\frac{13}{72}\frac{l^2}{r^2}\right]\simeq 37 \text{ E} . \tag{40}$$

The l^2/r^2 term is the finite base line term of the gradiometer. Here the Pb brick has been approximated as a point mass. Its actual geometry and size should be taken into account for a precise calibration. The measured peak-to-peak dc current change is 2.3 nA. This current corresponds to (38 ± 2) E, in good agreement with Eq. (40), if the accelerometer mode calibration of Sec. IV C is used.

For Fig. 15(c), the brick was moved in the same way but along a direction roughly perpendicular to the gradiometer axis. The expected signal, if the Pb brick were a point mass and were located accurately, is given by

$$-\frac{GM}{r^3}\left[1-\frac{3}{8}\frac{l^2}{r^2}\right]\simeq -34 \text{ E} . \tag{41}$$

The value measured from Fig. 15(c) is (-25 ± 2) E. An error of 10% in r and in angular orientation could produce this gradient error of 30%. The brick has a long rectangular shape so that a substantial amount of its mass was at other orientations and at larger separations relative to the gradiometer.

The experiments have been qualitatively repeated at a few other orientations relative to the gradiometer axis. The results agree with what we expect from the tensor property of the single-axis gradiometer. The validity of a gravity signal has therefore been substantiated.

The random error seen in Fig. 15 is of the order of 1 E. Taking into account the bandwidth of measurement, 0.16 Hz, one can estimate the noise spectral density to be approximately 2.5 E $\text{Hz}^{-1/2}$. This is consistent with the level recorded on the spectrum analyzer at the signal frequency of 0.03 Hz (see Fig. 10). Similar "mass flyby" experiments were performed with room temperature gravity gradiometers.[14—16] Analysis of the reported data indicates noise levels of 5—15 E $\text{Hz}^{-1/2}$ for these instruments. The noise levels in these experiments represent only upper bounds of the instrument noise levels since performance of the instruments was limited by the environmental noise in most cases. It is clear that, although the intrinsic noise level of the cryogenic instrument is many orders of magnitude superior to those of the room-temperature devices, better control or more efficient rejection of the environmental noise must be performed in order to fully utilize its potential sensitivity.

C. Inverse-square law experiment

The most impressive demonstration that the gravity gradiometer output is a genuine gravity gradient signal comes from the inverse-square law data[5,7] in which the angular pattern of the gravity gradient tensor is checked. For this experiment, the sensitive axis of the single-axis gradiometer was turned into three orthogonal directions by rotating the entire experimental cryostat on a turntable incrementally by 120° around the vertical axis while the gradiometer was suspended in the umbrella angle. The resulting three outputs and their sum are plotted in Fig. 16 after signal averaging over 500 pendulum periods. The peak-to-peak amplitudes of the three outputs agree with the theoretical formula

$$\Delta\Gamma_{ii}=\frac{GM}{r^3}\frac{3\Delta r}{r}\cos 2\psi_i , \tag{42}$$

where $r=2.3$ m is the average distance between the Pb sphere and the gradiometer, $\Delta r=0.84$ m is the peak-to-peak amplitude of swing, and $\psi_i=120°\,(i-1)-3.7°$ is the angle that the projection of the ith sensitive axis onto the horizontal plane makes with the line of sight between the detector and the source.

The sum of the right-hand side of Eq. (42) over $i=1$—3 vanishes as expected from the Poisson equation for Newtonian gravity, Eq. (12) of paper I:

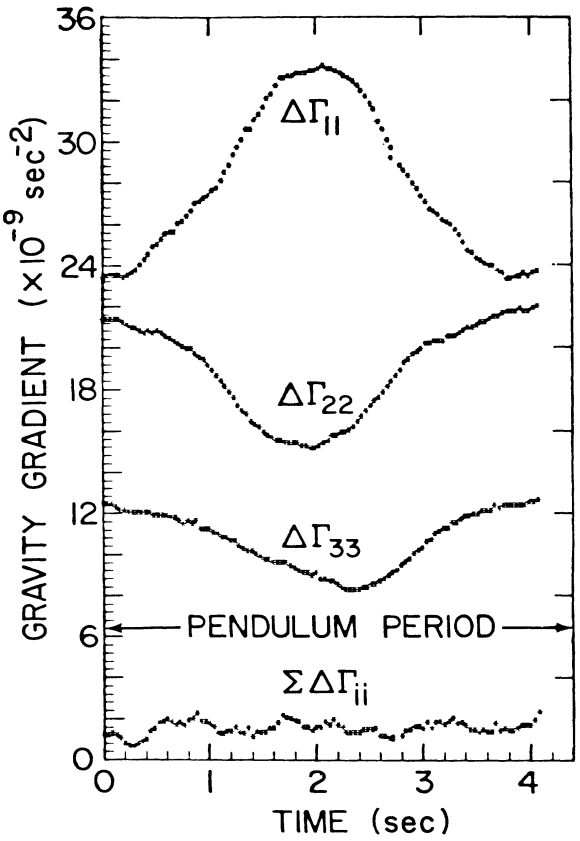

FIG. 16. Inverse-square law data (dc level is arbitrary).

$$\sum_i \Delta\Gamma_{ii}=0\ . \tag{43}$$

The sum of the three orthogonal measurements, the bottom trace of Fig. 16, verifies this condition within experimental uncertainty:

$$\sum_i \Delta\Gamma_{ii}=(+0.15\pm0.23)\times10^{-9}\ \mathrm{sec}^{-2}\ . \tag{44}$$

The signal and noise in this result have been analyzed carefully and published as a *null test of the gravitational inverse-square law.*[5] Within the inverse square law, the mutual cancellation of the signals in three arbitrary orthogonal directions is strong proof that the instrument is really measuring genuine gravity gradient signals since it will be highly unlikely that other error signals also satisfy the condition (43).

VII. SUMMARY AND CONCLUSION

A superconducting gravity gradiometer has been constructed and evaluated very carefully. Both the signal transfer and noise characteristics of the device agree closely with the theoretical model. Practical error sources have been identified experimentally as well as analytically. Although the instrument has only been tested on a passive platform without any feedback or error compensation, it has shown a performance level of 0.3—0.7 $\mathrm{E\,Hz^{-1/2}}$ above 0.1 Hz, outside the region where the noise level deteriorates due to effects which appear to be associated with the temperature fluctuations of the instrument. The minimum noise level exhibited by the cryogenic gradiometer, 0.1 $\mathrm{E^2\,Hz^{-1}}$ in a narrow frequency band around 0.15 Hz, surpasses the value achieved in a sophisticated room temperature gravity gradiometer[14] by 3 orders of magnitude in power. Further reduction of noise should be possible by improving the alignment of component accelerometers or by actively stabilizing the gradiometer platform against horizontal accelerations. The temperature of the He bath could also be controlled to reduce the low-frequency noise of the instrument.

The instrument has been used to carry out a preliminary null test of Newton's inverse-square law of gravitation. The successful operation of the superconducting gradiometer in a rather simple setting demonstrates that the macroscopic quantum-mechanical phenomenon exhibited in superconductivity *can* be taken advantage of to meet many practical challenges posed by sensitive gravity measurements. The careful modeling of the instrument and its experimental confirmation establishes the feasibility of constructing a more advanced superconducting gravity gradiometer and carrying out precision gravity experiments.

Guided by the theoretical and experimental work reported in papers I and II, we are in the process of constructing a three-axis superconducting gravity gradiometer of an advanced design.[6,17] The new gradiometer incorporates additional technical innovations such as a "superconducting negative spring" and a "three-dimensional residual common mode balance" as well as the cold damping and force rebalance feedbacks to achieve an instrument noise level of $10^{-4}\ \mathrm{E\,Hz^{-1/2}}$ (Ref. 18). Such a sensitive and stable gradiometer will find important applications in inertial navigation and geophysical survey as well as in fundamental physics experiments. A series of precision inverse-square law tests as well as tests of general relativistic effects are planned with this instrument both in the terrestrial laboratory and in space.[19,20] The work presented here lays the ground work for further development of superconducting technology for gravity and acceleration measurements.

ACKNOWLEDGMENTS

We wish to acknowledge valuable contributions from Dr. Evan Mapoles, Dr. Daniel DeBra, and Dr. Jean-Paul Richard in the design of the superconducting gravity gradiometer. We thank Bob Horne and Frank Desrosier for their skillful mechanical work in the fabrication of the gradiometer and supporting hardware. The 1.6-ton lead pendulum was constructed with the material provided by the National Bureau of Standards, Gaithersburg, Maryland. We have also benefited from collaboration with Qin Kong and Joel Parke. This work was supported by NASA under Contract No. NAS 8-33822.

APPENDIX A: VIBRATION ISOLATION BY PENDULUM ACTION

Isolation of horizontal vibrations by pendulum action has been analyzed in Ref. 7 by treating the angular motion of the pendulum in time domain. Here we treat the problem in frequency domain. For a platform suspended in a stationary laboratory, the angular amplitude of the pendulum is of the order of 10^{-6} rad at its resonance frequency. Effects that arise from second-order contributions in angle will therefore be negligible in general.

A. Vibration isolation of an accelerometer

We first consider a single accelerometer mounted on a platform suspended by a *symmetric* pendulum of effective length l_p, the distance between the pivot point and the "center of percussion" of the platform [see Fig. 17(a)].

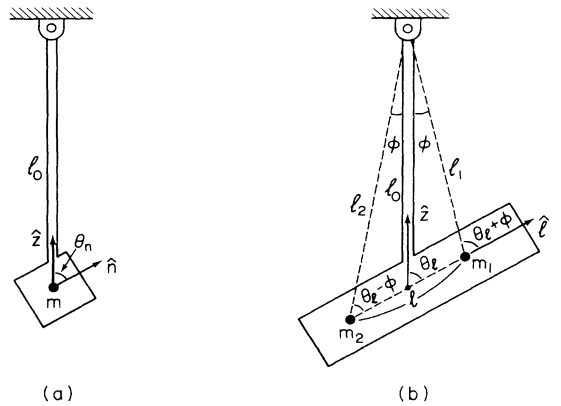

FIG. 17. Pendulum suspension of (a) an accelerometer and (b) a gradiometer.

The effective length of the pendulum is defined from ω_p, the degenerate (angular) resonance frequency of the swinging mode, by

$$l_p \equiv g_E/\omega_p{}^2 . \tag{A1}$$

Let the center of mass of the accelerometer proof mass be located at a vertical distance l_0 below the pivot point with its sensitive axis defined by $\hat{\mathbf{n}}$. We further assume a "perfectly rigid" pendulum in which the pendulum mass and the suspension rod form a perfectly rigid body and the pivot is perfectly rigid for linear motions while it is perfectly soft for angular motions. This condition could be approached in practice by designing the pendulum with the resonance frequencies of unwanted modes high compared to the swinging mode frequency ω_p.

Under these assumptions, the accelerometer platform is completely isolated from the angular motions of the ceiling from which the pendulum is suspended. This isolation is independent of frequency although, in practice, finite rigidity for the torsional mode tends to make the pendulum a low-pass filter for the torsional jitter of the external world. No attenuation is expected for vertical vibrations. Since linear accelerations can be balanced out in one direction in a gradiometer, our interest is in the extent to which horizontal accelerations $\mathbf{a}_h(t)$ can be rejected by means of the pendulum action.

Let us denote the horizontal displacements of the pivot point and the center of percussion of the platform by $\mathbf{R}_h(t)$ and $\mathbf{r}_h(t)$, respectively. Then, the equation of motion of the pendulum can be written as

$$\ddot{\mathbf{r}}_h + \tau_p{}^{-1}(\dot{\mathbf{r}}_h - \dot{\mathbf{R}}_h) + \omega_p{}^2(\mathbf{r}_h - \mathbf{R}_h) = 0 . \tag{A2}$$

Taking a Fourier transform of this equation, one finds

$$\mathbf{r}_h(\omega) = \frac{\omega_p{}^2 + j\omega\tau_p{}^{-1}}{\omega_p{}^2 - \omega^2 + j\omega\tau_p{}^{-1}} \mathbf{R}_h(\omega) . \tag{A3}$$

The horizontal acceleration of the platform is therefore

$$\mathbf{a}_h(\omega) = -\omega^2 \mathbf{r}_h(\omega) = \frac{\omega_p{}^2 + j\omega\tau_p{}^{-1}}{\omega_p{}^2 - \omega^2 + j\omega\tau_p{}^{-1}} \mathbf{A}_h(\omega) , \tag{A4}$$

where $\mathbf{A}_h(\omega) \equiv -\omega^2 \mathbf{R}_h(\omega)$ represents the external acceleration.

The resulting angular displacement of the platform in the Earth coordinate system is given by

$$\boldsymbol{\theta}_p(\omega) = \frac{1}{l_p}[\mathbf{r}_h(\omega) - \mathbf{R}_h(\omega)] \times \hat{\mathbf{z}} , \tag{A5}$$

to the first order in $\boldsymbol{\theta}_p$. Substitution of Eq. (A3) into Eq. (A5) leads to

$$\boldsymbol{\theta}_p(\omega) = \frac{-1}{\omega_p{}^2 - \omega^2 + j\omega\tau_p{}^{-1}} \frac{1}{l_p} \mathbf{A}_h(\omega) \times \hat{\mathbf{z}} , \tag{A6a}$$

$$\boldsymbol{\Omega}_p(\omega) = j\omega\boldsymbol{\theta}_p(\omega) = \frac{-j\omega}{\omega_p{}^2 - \omega^2 + j\omega\tau_p{}^{-1}} \frac{1}{l_p} \mathbf{A}_h(\omega) \times \hat{\mathbf{z}} , \tag{A6b}$$

$$\boldsymbol{\alpha}_p(\omega) = -\omega^2 \boldsymbol{\theta}_p(\omega) = \frac{\omega^2}{\omega_p{}^2 - \omega^2 + j\omega\tau_p{}^{-1}} \frac{1}{l_p} \mathbf{A}_h(\omega) \times \hat{\mathbf{z}} . \tag{A6c}$$

Notice here that $\boldsymbol{\Omega}_p(\omega)$ represents the angular velocity of the platform with respect to Earth.

The total specific force acting on the accelerometer proof mass is

$$g'(t) = \hat{\mathbf{n}}(t) \cdot [\mathbf{g}_E - \mathbf{a}_{h0}(t)] , \tag{A7}$$

where $\mathbf{a}_{h0}(t)$ is the horizontal acceleration of the platform at the proof mass, which is given by a weighted average of $\mathbf{A}_h(t)$ and $\mathbf{a}_h(t)$:

$$\mathbf{a}_{h0}(t) = \left[1 - \frac{l_0}{l_p}\right] \mathbf{A}_h(t) + \frac{l_0}{l_p} \mathbf{a}_h(t) . \tag{A8}$$

The Fourier transform of Eq. (A7) is

$$g(\omega) = \boldsymbol{\theta}_p(\omega) \times \hat{\mathbf{n}} \cdot \mathbf{g}_E - \hat{\mathbf{n}} \cdot \mathbf{a}_{h0}(\omega) , \tag{A9}$$

to the first order in $\boldsymbol{\theta}_p$, where the vector identity (A11a) of paper I has been utilized to obtain $\hat{\mathbf{n}}(\omega)$ and

$$\mathbf{a}_{h0}(\omega) = \frac{\omega_p{}^2 + j\omega\tau_p{}^{-1} - (1 - l_0/l_p)\omega^2}{\omega_p{}^2 - \omega^2 + j\omega\tau_p{}^{-1}} \mathbf{A}_h(\omega) . \tag{A10}$$

Substitution of $\mathbf{g}_E = -g_E \hat{\mathbf{z}}$ into Eq. (A9) gives the form

$$g(\omega) = \hat{\mathbf{n}} \cdot [g_E \boldsymbol{\theta}_p(\omega) \times \hat{\mathbf{z}} - \mathbf{a}_{h0}(\omega)] . \tag{A11}$$

Now, we substitute Eqs. (A6a) and (A10) to obtain

$$g(\omega) = \frac{(1 - l_0/l_p)\omega^2 - j\omega\tau_p{}^{-1}}{\omega_p{}^2 - \omega^2 + j\omega\tau_p{}^{-1}} \hat{\mathbf{n}} \cdot \mathbf{A}_h(\omega) , \tag{A12}$$

where the main contributions to the two terms in Eq. (A11) have canceled each other by Eq. (A1). Namely, the horizontal acceleration of the proof mass is almost exactly balanced out by the modulation of Earth's gravity which results from the tilt of the platform.

According to Eq. (A12), residual errors in the horizontal vibration isolation arises from two sources—misposition of the accelerometer proof mass ($l_0 \neq l_p$) and damping ($Q_p = \omega_p \tau_p < \infty$). When $l_0 = l_p$ is chosen, the attenuation obtained by the pendulum action goes as

$$\left| \frac{g(\omega)}{\hat{\mathbf{n}} \cdot \mathbf{A}_h(\omega)} \right| \simeq \begin{cases} (\omega/\omega_p) Q_p{}^{-1}, & \omega \ll \omega_p , \quad \text{(A13a)} \\ 1, & \omega = \omega_p , \quad \text{(A13b)} \\ (\omega_p/\omega) Q_p{}^{-1}, & \omega \gg \omega_p . \quad \text{(A13c)} \end{cases}$$

At resonance, the platform is actually driven to an amplitude Q_p times larger, as can be seen from Eq. (A10), and the pendulum action balances the horizontal acceleration to $Q_p{}^{-1}$ so that the net gain will be unity. Away from

resonance, the horizontal acceleration is attenuated by Q_p^{-1} times a frequency factor which helps the isolation further. Thus, we have proved that the pendulum suspension indeed provides *wideband* isolation of an accelerometer from horizontal accelerations as well as tilts except in the immediate vicinity of its resonance frequency.

We have assumed symmetry of the pendulum frequency in two horizontal directions for simplicity. Equation (A12) shows that this assumption is not necessary for the operation of the pendulum action. Since the accelerometer is not sensitive to a horizontal acceleration perpendicular to $\hat{\mathbf{n}}$, the foregoing analysis will be valid as long as l_0 is chosen to be equal to the effective length of the pendulum l_p in the vertical plane which includes $\hat{\mathbf{n}}$.

B. Vibration isolation of a gravity gradiometer

We now turn to a gradiometer mounted on a platform under pendulum suspension [Fig. 17(b)]. In general, the two component accelerometers have slightly different sensitive axes $\hat{\mathbf{n}}_1$ and $\hat{\mathbf{n}}_2$ and are located at different distances l_1 and l_2 from the pivot point. The distance between the pivot point and the center of percussion, which is near the midpoint between the two proof masses, is denoted by l_0. Since a very small differential acceleration signal is sought for in general, errors coupled through misalignments of the sensitive axes will have to be examined carefully. The result of a general analysis of the misalignment errors is given by Eq. (A6b) of paper I, which can be written in the form

$$\delta\Gamma_{\hat{\mathbf{n}}+\hat{l}}(t)=\frac{1}{l}\delta\hat{\mathbf{n}}_-\cdot[\mathbf{g}_E-\mathbf{a}(t)]+(\delta\hat{\mathbf{n}}_{+\hat{\mathbf{n}}}+\delta\hat{l})\cdot[\vec{\Gamma}_E-\boldsymbol{\Omega}(t)\boldsymbol{\Omega}(t)]\cdot\hat{\mathbf{n}}+\delta\hat{\mathbf{n}}_{+\hat{l}}\times\hat{\mathbf{n}}\cdot\boldsymbol{\alpha}(t)\ , \tag{A14}$$

where l is the base line of the gradiometer, and $\delta\hat{\mathbf{n}}_-$, $\delta\hat{\mathbf{n}}_{+\hat{l}}$, $\delta\hat{\mathbf{n}}_{+\hat{\mathbf{n}}}$, $\delta\hat{l}$ are the misalignment and misorientation vectors defined by Eqs. (92)—(94) of paper I. The gravity gradient ($\vec{\Gamma}_E$) term can be ignored in comparison with the gravity ($\mathbf{g}_E$) term, and the correction term to centrifugal acceleration can be dropped since the full centrifugal acceleration is regarded as a separate error source in paper II.

Upon Fourier transformation, Eq. (A14) becomes, to the first order in θ_p,

$$\delta\Gamma_{\hat{\mathbf{n}}+\hat{l}}(\omega)=\frac{1}{l}\delta\hat{\mathbf{n}}_-\cdot[g_E\theta_p(\omega)\times\hat{\mathbf{z}}-\mathbf{a}_{h0}(\omega)]+\delta\hat{\mathbf{n}}_{+\hat{l}}\times\hat{\mathbf{n}}\cdot\boldsymbol{\alpha}_p(\omega)\ , \tag{A15}$$

where the second term in Eq. (A14) has been ignored and appropriate quantities for the pendulum suspension have been substituted into the linear and angular accelerations. Here $\mathbf{a}_{h0}(\omega)$ is the horizontal acceleration of the midpoint between the two accelerometers. In deriving Eq. (A15), use has been made of the relationship between the accelerations at the two accelerometers, $\mathbf{a}_{hk}(\omega)$ and $\mathbf{a}_{h0}(\omega)$:

$$\left|\frac{\mathbf{a}_{hk}(\omega)}{\mathbf{a}_{h0}(\omega)}\right|=\frac{l_k}{l_0}=\frac{\sin\theta_l}{\sin[\theta_l-(-1)^k\phi]}\ , \tag{A16}$$

to obtain a perfect balance of the accelerations along the direction $\hat{l}$:

$$l\cdot[\mathbf{a}_{h2}(\omega)-\mathbf{a}_{h1}(\omega)]=a_{h2}(\omega)\sin(\theta_l-\phi)-a_{h1}(\omega)\sin(\theta_l+\phi)=0\ . \tag{A17}$$

The angles θ_l and ϕ are defined in Fig. 17(b). In addition we have assumed $l_0\gg l$ to approximate

$$\tfrac{1}{2}\delta\hat{\mathbf{n}}_-\cdot[\mathbf{a}_{h2}(\omega)+\mathbf{a}_{h1}(\omega)]\simeq\delta\hat{\mathbf{n}}_-\cdot\mathbf{a}_{h0}(\omega)\ . \tag{A18}$$

Substitution of Eqs. (A6) and (A10) into Eq. (A15) results in

$$\delta\Gamma_{\hat{\mathbf{n}}+\hat{l}}(\omega)=\frac{(1-l_0/l_p)\omega^2-j\omega\tau_p^{-1}}{\omega_p^2-\omega^2+j\omega\tau_p^{-1}}\frac{1}{l}\delta\hat{\mathbf{n}}_-\cdot\mathbf{A}_h(\omega)+\frac{\omega^2}{\omega_p^2-\omega^2+j\omega\tau_p^{-1}}\frac{1}{l_p}\delta\hat{\mathbf{n}}_{+\hat{l}}\times\hat{\mathbf{n}}\cdot\mathbf{A}_h(\omega)\times\hat{\mathbf{z}}\ . \tag{A19}$$

The first term in Eq. (A19) is again minimized by choosing $l_0=l_p$; i.e., by locating the center of the gradiometer at the center of percussion of the platform. In this case, however, the horizontal acceleration couples in through the second term which represents the effect of the induced angular acceleration. In order to balance out $\mathbf{A}_h(\omega)$ in the two terms, l_0 should rather be chosen to satisfy

$$\left[\frac{l_p-l_0}{l}\right]\delta\hat{\mathbf{n}}_-+(\hat{\mathbf{n}}\cdot\hat{\mathbf{z}})\delta\hat{\mathbf{n}}_{+\hat{l}}-(\delta\hat{\mathbf{n}}_{+\hat{l}}\cdot\hat{\mathbf{z}})\hat{\mathbf{n}}=0\ . \tag{A20}$$

Since there are three independent components in this equation, it is impossible in general to satisfy this equation by adjusting a single parameter l_0 even if $\delta\hat{\mathbf{n}}_-$ and $\delta\hat{\mathbf{n}}_{+\hat{l}}$ are predetermined. Therefore, in order to obtain a wideband rejection of the horizontal accelerations in a gradiometer by means of the pendulum suspension, a sufficiently small value of $\delta\hat{\mathbf{n}}_{+\hat{l}}$ is required.

An additional error term is generated through the centrifugal acceleration of the gradiometer proof masses induced by $\mathbf{A}_h(\omega)$. This error is given by Eq. (A10) of paper I:

$$\delta\Gamma_{\vec{C}}(\omega)=-2\{(\hat{\mathbf{n}}\cdot\boldsymbol{\Omega}_E)[\hat{\mathbf{n}}\cdot\boldsymbol{\Omega}_p(\omega)]-\boldsymbol{\Omega}_E\cdot\boldsymbol{\Omega}_p(\omega)\}\ . \tag{A21}$$

Substitution of Eq. (A6b) into this equation yields

$$\delta\Gamma_{\vec{C}}(\omega)=\frac{j\omega}{\omega_p^2-\omega^2+j\omega\tau_p^{-1}}\frac{2}{l_p}[(\hat{\mathbf{n}}\cdot\boldsymbol{\Omega}_E)\hat{\mathbf{n}}-\boldsymbol{\Omega}_E]\cdot\mathbf{A}_h(\omega)\times\hat{\mathbf{z}}\ . \tag{A22}$$

A combination of Eqs. (A19) and (A22) gives the total residual error arising from $\mathbf{A}_h(\omega)$:

$$\delta\Gamma_h(\omega) = \frac{\omega^2\delta\hat{\mathbf{n}}_{+\hat{l}}\times\hat{\mathbf{n}}+j\omega 2[(\hat{\mathbf{n}}\cdot\boldsymbol{\Omega}_E)\hat{\mathbf{n}}-\boldsymbol{\Omega}_E]}{\omega_p{}^2-\omega^2+j\omega\tau_p{}^{-1}}\frac{1}{l_p}\mathbf{A}_h(\omega)\times\hat{\mathbf{z}} . \tag{A23}$$

Equation (A23) shows that the pendulum works as an attenuator with an attenuation factor proportional to $(l/l_p)|\delta\hat{\mathbf{n}}_{+\hat{l}}|$ and $(l/l_p)(\omega/\Omega_E)$, respectively, for each error term, plus a high-pass filter with the cutoff frequency ω_p. Therefore, for a gradiometer, the pendulum action *attenuates* the horizontal accelerations *at all frequencies, with the isolation becoming perfect as the signal frequency approaches dc.* This is usually sufficient because the signal bandwidth satisfies $\omega<\omega_p$ in most applications of a gradiometer. It is truly remarkable that the pendulum action accomplishes a *nearly perfect, passive* vibration isolation in two dimensions *near dc* because vibration isolation below 1 Hz is very difficult to achieve by means of conventional spring-mass isolators.

In the frequency range $\omega>\Omega_E/|\delta\hat{\mathbf{n}}_{+\hat{l}}|$, the centrifugal acceleration term can be ignored in comparison with the angular acceleration term so that

$$\delta\Gamma_h(\omega)\simeq h_\alpha(\omega)\frac{1}{l_p}\delta\hat{\mathbf{n}}_{+\hat{l}}\times\hat{\mathbf{n}}\cdot\mathbf{A}_h(\omega)\times\hat{\mathbf{z}} , \tag{A24}$$

where

$$h_\alpha(\omega)\equiv\frac{\omega^2}{\omega_p{}^2-\omega^2+j\omega\tau_p{}^{-1}} \tag{A25}$$

is the normalized transfer function for coupling of $\mathbf{A}_h(\omega)$ through induced angular acceleration. The absolute value of this function is plotted in Fig. 11 (solid line) for parameter values of $\omega_p/2\pi=0.32$ Hz and $Q_p=\omega_p\tau_p=300$. Also plotted in the figure (dotted line) for comparison is the absolute value of the transfer function for direct transmission of $\mathbf{A}_h(\omega)$ to the pendulum mass:

$$h_t(\omega)\equiv\frac{\omega_p{}^2+j\omega\tau_p{}^{-1}}{\omega_p{}^2-\omega^2+j\omega\tau_p{}^{-1}} , \tag{A26}$$

which is read from Eq. (A4). Thus, the pendulum itself responds to the horizontal acceleration as a low-pass filter with a frequency characteristic given by Eq. (A26). Equation (A6a) shows that the induced angular displacement has an almost identical frequency response which cancels the direct transmission term to approximately $Q_p{}^{-1}$. What is left over after this cancellation is the frequency characteristic of a high-pass filter given by Eq. (A25).

APPENDIX B: LOW-FREQUENCY NOISE OF THE GRADIOMETER

Gravity gradient signals of interest are usually at very low frequencies (10^{-4}–1 Hz). Excess low-frequency noise (red noise), which raises the overall instrument noise above the Brownian motion noise, is therefore of great concern in constructing a sensitive gravity gradiometer. Red noise in the gradiometer output can be generated by thermal and mechanical drift of the gradiometer, nonlinearities in the instrument, centrifugal acceleration of the platform, the $1/f$ noise, and drift of the detecting electronics, etc. One way of overcoming certain types of such low-frequency noise in an up conversion of the gravity gradient signal by rotating the instrument followed by a heterodyne detection of the modulated signal.[21] The rotation, however, increases the centrifugal acceleration and introduces additional dynamically induced noise sources. In this appendix we analyze how various error mechanisms contribute to the excess low-frequency noise for a nonrotating gravity gradiometer.

A. Temperature drift

Temperature coefficients of the superconducting gravity gradiometer have been derived in the Appendix of paper I. It has been found that the dominant effect comes from the functional dependence of the penetration depth $\lambda(T)$ on temperature T. The good thermal conductivity through the gradiometer body makes the differential temperature fluctuation $T_d(\omega)$ negligible compared to the common temperature fluctuation $T_c(\omega)$. The temperature-induced error can therefore be written as

$$\delta g_{d,T}(\omega)=h_{Tc}(\omega)T_c(\omega) , \tag{B1}$$

where

$$h_{Tc}(\omega)\equiv[\alpha_2^T(\omega_{2\lambda}{}^2-\omega^2)-\alpha_1^T(\omega_{1\lambda}{}^2-\omega^2)](1+\zeta)\frac{d\lambda}{dT} , \tag{B2}$$

and $\alpha_k^T,\omega_{k\lambda}{}^2$ are defined by Eqs. (A42) and (A45) of paper I, respectively, and $\zeta\lesssim 1$ is the modulation efficiency of the penetration depth for the pancake coils.

In the experiment, $i_k\simeq 0$ was chosen so that

$$\alpha_k^T\simeq\frac{L_{ka}-L_{kb}}{L_{ks}} , \tag{B3}$$

$$\omega_{k\lambda}\simeq\omega_{kM} . \tag{B4}$$

Substituting into Eq. (B2) the measured values of these parameters listed in Table I and

$$\frac{d\lambda}{dT}=\frac{2\lambda(0)}{T_0}\frac{(T/T_0)^3}{[1-(T/T_0)^4]^{3/2}}=9.7\times10^{-10}\ \mathrm{m/K} \tag{B5}$$

for Nb at $T=4.2$ K, one obtains

$$\epsilon_n^T(\omega)\equiv\frac{1}{l}h_{Tc}(\omega)=-2.9\times10^4\ \mathrm{E\,K^{-1}},\quad \omega\ll\omega_{kM} , \tag{B6}$$

for the present gradiometer.

Thus far the temperature-induced error has been analyzed in the frequency domain. Although this description is complete, it is often convenient to measure and compensate for the temperature effect in real time. No-

tice that $h_{Tc}(\omega)$ becomes independent of ω when $\omega \ll \omega_{k\lambda}$. Therefore, for a slow drift with $t \gg \omega_{k\lambda}^{-1}$, one expects a linear relationship:

$$\delta g_{d,T}(t) = h_{Tc} T_c(t) , \tag{B7}$$

where

$$h_{Tc} \simeq h_{Tc} \quad (\omega = 0) . \tag{B8}$$

The observed noise $T_c(t)$ in time domain can be related to the power spectral density $S_T(f)$ by a standard formula for the digital FFT (fast Fourier transform):[22]

$$S_T(f) = \left\langle \frac{2}{\tau} \left| \int_{-\tau/2}^{\tau/2} T_c(t) e^{-j2\pi f t} dt \right|^2 \right\rangle , \tag{B9}$$

where τ is the sample length. For a linear drift,

$$T_c(t) = at , \tag{B10}$$

this equation yields

$$S_T(f) = \frac{\tau}{4\pi^2} \frac{\langle a^2 \rangle}{f^2} , \quad f > \frac{1}{\pi\tau} . \tag{B11}$$

Notice that the result depends on the choice of τ. Combination of Eqs. (B1) and (B9) leads to

$$S_{\Gamma,T}(f) = (\epsilon_n^T)^2 \frac{\tau}{4\pi^2} \frac{\langle a^2 \rangle}{f^2} . \tag{B12}$$

Thus, a linear temperature drift causes a $1/f^2$ power spectrum at the gradiometer output.

In the experiment the gradiometer was thermally isolated from the He bath through vacuum. The large heat capacity of the gradiometer body and the low conductivity through the electrical leads and the residual He gas formed a low-pass *RC* filter for heat flow with a transfer function:

$$h_F(f) = \frac{1}{1 + j2\pi f \tau_F} , \tag{B13}$$

where τ_F is the filter time constant. In a high vacuum, τ_F exceeded 10^3 sec. In fact, we had to maintain a pressure level of approximately 10^{-4} mm Hg to bring the gradiometer assembly into thermal equilibrium with the He bath in a reasonable time after turning on heat switches on the gradiometer. A typical response time used was $\tau_F \simeq 500$ sec. A Ge thermometer was mounted on the gradiometer assembly to measure $T_c(t)$. However, the thermometer did not have enough resolution to track the stable temperature of the gradiometer. All we could determine directly is a rough estimate of the experimental upper limit, 2×10^{-4} K h^{-1}, for dT_c/dt so that

$$a_{\rm rms} \lesssim 5.6 \times 10^{-8} \text{ K sec}^{-1} . \tag{B14}$$

Substituting $\tau = 125$ sec, the sampling time used for the spectrum analyzer, and Eqs. (B6) and (B14) into Eq. (B12), we obtain

$$[S_{\Gamma,T}(f)]^{1/2} \lesssim 2.9 \times 10^{-2} \text{ E Hz}^{-1/2} \left[\frac{0.1 \text{ Hz}}{f} \right] . \tag{B15}$$

In a separate experiment,[8] the temperature of the He bath was measured by dipping a "superconducting penetration depth thermometer" of the type similar to the one described in Ref. 23 into a storage Dewar. The Fourier analysis of this data is shown in Fig. 18. This data indicates that, in the frequency range of interest between 10^{-2} and 10^{-1} Hz, the spectrum can be described by

$$[S_T(f)]_{\rm bath}^{1/2} = 1.1 \times 10^{-4} \text{ K Hz}^{-1/2} \left[\frac{0.1 \text{ Hz}}{f} \right] . \tag{B16}$$

Since the exact behavior of the temperature noise should depend on the characteristics of the Dewar and the insert as well as the barometric pressure fluctuation in the laboratory, this data should be interpreted as an *order-of-magnitude estimate* for the temperature noise in our experiment. Combining Eq. (B16) with Eqs. (B6) and (B13), one finds

$$[S_{\Gamma,T}(f)]^{1/2} \simeq \frac{1}{2\pi f \tau_F} \epsilon_n^T [S_T(f)]_{\rm bath}^{1/2}$$

$$= 1.0 \times 10^{-2} \text{ E Hz}^{-1/2} \left[\frac{0.1 \text{ Hz}}{f} \right]^2 . \tag{B17}$$

This estimate falls within the approximate limit given by Eq. (B15).

B. General consideration of nonlinear effects

Since nonlinearity is a higher-order effect, the most important error coupling mechanisms will involve the second-order nonlinearity. Thus we restrict our discussion to a nonlinear behavior of the form

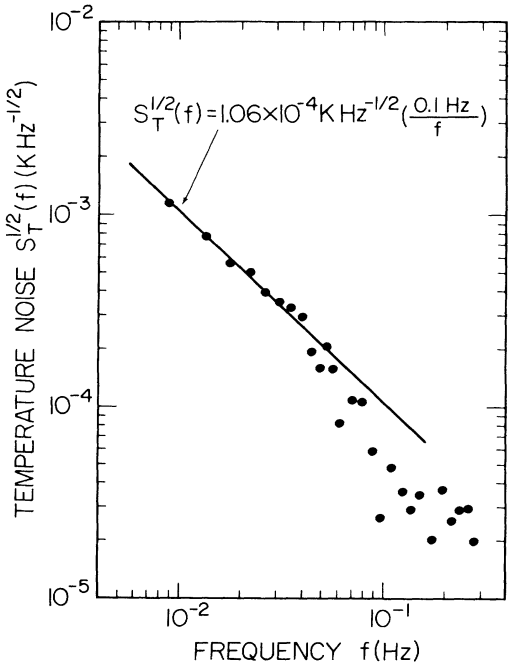

FIG. 18. Temperature noise spectrum of a liquid-helium bath.

$$\delta g_{d,N}(t)=\int_{-\infty}^{\infty} h_N(t-t')g^2(t')dt' . \tag{B18}$$

The driving acceleration $g(t)$ could be either $g_c(t)$ or $g_d(t)$. In this section we wish to obtain a relationship between the Fourier components $g(\omega)$ and $\delta g_{d,N}(\omega)$, and investigate specifically how the wideband noise $g(\omega)$ contributes to a low-frequency divergence in $\delta g_{d,N}(\omega)$ through the squaring process.

The Fourier transform of Eq. (B18) is

$$\delta g_{d,N}(\omega)=h_N(\omega)G(\omega) , \tag{B19}$$

where $G(\omega)$ is the Fourier transform of

$$G(t)\equiv g^2(t) . \tag{B20}$$

In experiments, one usually measures *one-sided* power spectral densities as functions of $f=\omega/2\pi\geq 0$ rather than ω. Equation (B19) implies a relationship for such power spectral densities:

$$S_{\Gamma,N}(f)=\frac{1}{l^2}\,|\,h_N(f)\,|^2 S_G(f) , \tag{B21}$$

where $h_N(f)=h_N(\omega)$ and $S_G(f)$ is related to $S_g(f)$ by a convolution:[24]

$$\tilde{S}_G(f)=\int_{-\infty}^{\infty}\tilde{S}_g(f')\tilde{S}_g(f-f')df' . \tag{B22}$$

The tilde represents two-sided spectral densities with a property:

$$\tilde{S}(-f)=\tilde{S}(f)=\tfrac{1}{2}S(f),\quad f\geq 0 . \tag{B23}$$

For a sinusoidal function with *random phase,*

$$g(t)=g\cos(2\pi f_0 t+\theta) , \tag{B24}$$

it is straightforward to show[25]

$$\tilde{S}_g(f)=\tfrac{1}{4}g^2[\delta(f-f_0)+\delta(f+f_0)] , \tag{B25}$$

$$\tilde{S}_G(f)=\tfrac{1}{16}g^4[\delta(f-2f_0)+4\delta(f)+\delta(f+2f_0)] . \tag{B26}$$

In practice, the δ functions in these equations are replaced by continuous functions with *finite peaks and widths* due to the finite sample length τ used in the computation of the spectral densities. Denoting this narrow-band response function with a subscript τ, the one-sided spectral densities can be written as

$$S_g(f)=\tfrac{1}{2}g^2\delta_\tau(f-f_0) , \tag{B27}$$

$$S_G(f)=\tfrac{1}{8}g^4[2\delta_{\tau/2}(f)+\delta_{\tau/2}(f-2f_0)] , \tag{B28}$$

where the line broadening by a factor 2 that takes place in the squaring operation[24] has been indicated by $\tau/2$. Notice that the factor $\frac{1}{2}$ in front of g^2 comes from the assumption that the phase θ of the signal is random. For a signal in phase with the reference signal, $g^2/2$ must be replaced by g^2 in Eqs. (B27) and (B28).

The exact line shape $\delta_\tau(f)$ depends on the window function employed in the Fourier analysis. A simple box-car shape window yields

$$\delta_\tau(f)=\delta_\tau^B(f)\equiv\int_{-\tau/2}^{\tau/2}e^{-j2\pi ft}dt=\frac{\sin(\pi f\tau)}{\pi f} . \tag{B29}$$

In the experiment, a Hanning window function[25] with the characteristic

$$\delta_\tau^H(f)\equiv\tfrac{1}{4}\delta_\tau^B\left[f-\frac{1}{\tau}\right]+\tfrac{1}{2}\delta_\tau^B(f)+\tfrac{1}{4}\delta_\tau^B\left[f+\frac{1}{\tau}\right] \tag{B30}$$

was used. Substitution of Eq. (B29) into Eq. (B30) leads to

$$\delta_\tau(f)=\delta_\tau^H(f)=\frac{\sin(\pi f\tau)}{2\pi f}\frac{1}{1-(f\tau)^2} . \tag{B31}$$

Notice that the Hanning filter produces a tail that goes as f^{-3}.

In the frequency range $2/\tau\lesssim f\lesssim f_0$, Eq. (B28) can now be approximated as

$$S_G(f)\simeq\frac{g^4}{4\pi\tau^2}\frac{1}{f^3} . \tag{B32}$$

In the general case when $S_g(f)$ is continuous, $g^2/2$ must be replaced by an integral of $S_g(f)$ over all frequencies so that

$$S_G(f)\simeq\frac{2}{\pi\tau^2}\frac{1}{f^3}\left[\int_0^\infty S_g(f')df'\right]^2 . \tag{B33}$$

Substituting this into Eq. (B21), one obtains the final result

$$[S_{\Gamma,N}(f)]^{1/2}\simeq\left[\frac{2}{\pi}\right]^{1/2}\frac{1}{l\tau}\frac{1}{f^{3/2}}\,|\,h_N(f)\,|\int_0^\infty S_g(f')df' . \tag{B34}$$

Notice that $S_{\Gamma,N}(f)$ can be reduced by increasing the sample length τ.

The nonlinearity coefficient $|\,h_N(f)\,|$ can be measured by driving the system with a sinusoidal acceleration at the frequency $f/2$:

$$g_F(t)=g_F\cos(\pi ft+\theta_F) \tag{B35}$$

and observing the resulting gradient at its second harmonic f:

$$\Gamma_S(t)=\frac{1}{l}g_S\cos(2\pi ft+\theta_s) . \tag{B36}$$

From the foregoing analysis it is easily seen that

$$g_S=\tfrac{1}{2}\,|\,h_N(f)\,|\,g_F{}^2 . \tag{B37}$$

The value of $|\,h_N(f)\,|$ obtained from this relationship could then be substituted into Eq. (B34).

C. Nonlinearities of the instrument

A general expression of the nonlinearity errors was given in paper I:

$$\delta g_{d,N}(\omega)=h_{cc}(\omega)G_{cc}(\omega)+h_{dd}(\omega)G_{dd}(\omega)+h_{cd}(\omega)G_{cd}(\omega) , \tag{B38}$$

where $G_{cc}(\omega)$, $G_{dd}(\omega)$, and $G_{cd}(\omega)$ are the Fourier transforms of $[g_c(t)]^2$, $[g_d(t)]^2$, and $g_c(t)g_d(t)$. The

derivation of the nonlinearity coefficients in this equation requires knowledge of experimental details.

We divide nonlinear mechanisms into three classes: (1) the instrument scale factor nonlinearity *internal* to the gradiometer, (2) dynamical nonlinear effects in which second-order terms are produced by the finite compliance of the gradiometer structure in undesirable directions, and (3) nonlinear effects of the platform. The first class of nonlinearity can be overcome by *linearizing* the gradiometer by means of a "force rebalance" feedback; i.e., by operating the gradiometer as a null detector in a feedback circuit. This method, however, will not suppress the latter two classes of nonlinearity errors inasmuch as these nonlinear effects are produced *external* to the instrument. In the pendulum-suspended platform, the third class of nonlinearity is produced by the centrifugal acceleration of the platform. In this section we discuss the first two classes of nonlinearity, deferring the treatment of the third class to the following section.

The *scale factor nonlinearity* can come from a failure of Hooke's law in the mechanical front end ($\partial x/\partial g$), from a nonlinear response of the transducer ($\partial i/\partial x$), and from nonlinearity in the gain of the amplifier ($\partial V/\partial i$) (see Fig. 1 of paper I). Since the SQUID operates in a negative feedback mode, it is a highly linear device and $\partial V/\partial i$ can be regarded as a constant. Further, the "cantilever" suspension spring for the proof masses has been specially designed to achieve a high degree of linearity along the sensitive axis. However, the transfer function $\partial i/\partial x$ of the superconducting transducer is intrinsically nonlinear, as can be seen in Eqs. (19), (25), and (32) of paper I. The second-order terms in the transducer transfer functions vanish if $L_a=L_b$ (symmetric coils) and $i=0$ (absence of symmetric current). The first condition, however, is difficult to satisfy in practice because the spacings between the coils and the surfaces of the proof masses are not easily matched.

In order to obtain relationships between the nonlinearity coefficients of the component acceleration transducers and of the gradiometer, we expand the current responses $i_k(t)$ of individual transducers as functions of driving accelerations $g_k(t)$:

$$\begin{aligned} i_k(t) &= h_{gi}^k g_k(t) + h_{Gi}^k g_k{}^2(t) + \cdots \\ &\equiv h_{gi}^k [g_k(t) + C_k^N g_k{}^2(t) + \cdots] . \end{aligned} \tag{B39}$$

Here an instantaneous response of the circuit has been assumed because of the low-frequency nature of the signals under investigation. The coefficients of the linear terms are matched by the common mode balance of the gradiometer so that the gradiometer output can be written as

$$\begin{aligned} g_d'(t) &= g_d(t) + (C_2^N - C_1^N)[g_c{}^2(t) + \tfrac{1}{4} g_d{}^2(t)] \\ &\quad + (C_1^N + C_2^N) g_c(t) g_d(t) + \cdots . \end{aligned} \tag{B40}$$

The transition from Eq. (B39) to Eq. (B40) is approximate because the electrical coupling between the two component transducers affects C_k^N, as they are combined into a gradiometer. Taking the Fourier transform of this equation and comparing it with Eq. (B38), one can identify

$$h_{cc}(\omega) \simeq 4 h_{dd}(\omega) \simeq C_2^N - C_1^N , \tag{B41a}$$

$$h_{cd}(\omega) \simeq C_1^N + C_2^N . \tag{B41b}$$

Notice that nonlinearity arises in the gradiometer even when the nonlinearity coefficients of the individual acceleration transducers are matched: i.e., $C_1^N = C_2^N$. The only way to eliminate the nonlinearity from the gradiometer scale factor is by making $C_1^N = C_2^N = 0$.

In the low-frequency limit, one can derive an *approximate* relationship:

$$C_k^N \simeq \frac{1}{\omega_{kM}{}^2} \frac{\Lambda}{L_{kp} + 2L_0} \frac{L_{ka} - L_{kb}}{L_{ka} + L_{kb}} \simeq \left[\frac{1}{\omega_M{}^2 \bar{d}_L} \frac{L_a - L_b}{L_a + L_b} \right]_k , \tag{B42}$$

where $\bar{d}_L$ is the average coil-to-proof-mass spacing. Substituting values listed in Table I, we find $C_1^N \simeq -7.5 \times 10^{-2}$ (m sec^{-2})$^{-1}$ and $C_2^N \simeq -1.7 \times 10^{-1}$ (m sec^{-2})$^{-1}$ so that

$$h_{cc}(\omega) \simeq 4 h_{dd}(\omega) \simeq -1.0 \times 10^{-1} \ (\text{m sec}^{-2})^{-1} , \tag{B43a}$$

$$h_{cd}(\omega) \simeq -2.5 \times 10^{-1} \ (\text{m sec}^{-2})^{-1} . \tag{B43b}$$

These values must be considered only as *order-of-magnitude estimates* in view of the approximations used in the derivation.

The *dynamic nonlinearity* of the instrument arises from the finite compliance of the gradiometer structure which allows the misalignment angles $\delta\hat{\mathbf{n}}_-$ and $\delta\hat{\mathbf{n}}_{+\hat{l}}$ to be driven by external accelerations $\mathbf{a}(t)$ or $\boldsymbol{\alpha}(t)$. From Eq. (A6b) of paper I, it is clear that a nonlinearity error arises if $\delta\hat{\mathbf{n}}_-$ or $\delta\hat{\mathbf{n}}_{+\hat{l}}$ is proportional to $\mathbf{a}(t)$ or $\boldsymbol{\alpha}(t)$. A bending mode of the structure can be excited by the perpendicular component of $\mathbf{a}(t)$ or $\boldsymbol{\alpha}(t)$ applied to the midpoint between the two accelerometers. The symmetry of the induced motion is such that the sensitive axes of the component accelerometers, $\hat{\mathbf{n}}_1$ and $\hat{\mathbf{n}}_2$, go out of alignment with respect to the base line vector $\hat{l}$, with opposite signs for $\mathbf{a}(t)$, and with an equal sign for $\boldsymbol{\alpha}(t)$. Therefore, the induced misalignments have functional forms given by

$$\delta\hat{\mathbf{n}}_-(t-t') = h_{\mathbf{aa}}(t-t') \mathbf{a}_\perp(t') , \tag{B44a}$$

$$\delta\hat{\mathbf{n}}_{+\hat{l}}(t-t') = h_{\boldsymbol{\alpha\alpha}}(t-t') \boldsymbol{\alpha}_\perp(t') , \tag{B44b}$$

where the history dependence of the coupling coefficients has resulted from the resonant response. Equation (A6b) of paper I is then generalized into

$$\begin{aligned} \delta g_{d,N}(t) = -\int_{-\infty}^{\infty} [& \delta\hat{\mathbf{n}}_-(t-t') \cdot \mathbf{a}(t') \\ & + l \delta\hat{\mathbf{n}}_{+\hat{l}}(t-t') \times \hat{\mathbf{n}} \cdot \boldsymbol{\alpha}(t')] dt' . \end{aligned} \tag{B45}$$

The general form (B18) is obtained if Eqs. (B44) are substituted into Eq. (B45). The corresponding equation for frequency domain is

$$\delta g_{d,N}(\omega) = h_{\mathbf{aa}}(\omega) G_{\mathbf{aa}}(\omega) + h_{\boldsymbol{\alpha\alpha}}(\omega) G_{\boldsymbol{\alpha\alpha}}(\omega) , \tag{B46}$$

where $G_{\mathbf{aa}}(\omega)$ and $G_{\boldsymbol{\alpha\alpha}}(\omega)$ are the Fourier transforms of $a_\perp{}^2(t)$ and $\alpha_\perp{}^2(t)$, respectively.

The coefficient $h_{\mathbf{aa}}(\omega)$ has been computed[26] for a circu-

lar tube that connects the two accelerometers. We only quote the result here:

$$|h_{aa}(\omega)| = \frac{3}{l\omega_B{}^2}\left[1+\frac{1}{Q_B{}^2}\left[\frac{\omega}{\omega_B}\right]^2\right]^{1/2} f\left[\frac{\omega}{\omega_B}\right], \tag{B47}$$

where

$$f(r)\equiv[(1-r^2)+Q_B{}^{-2}r^2]^{-1/2}. \tag{B48}$$

Here ω_B and Q_B represent the (angular) resonance frequency and the quality factor of the bending mode involved. A similar result is expected for $|h_{a\alpha}(\omega)|$.

Experimentally, the mounting cube for the gradiometer was made rather rigid so that $\omega_B/2\pi \gtrsim 300$ Hz. This gives upper limits for the nonlinearity error coefficients:

$$|h_{aa}(\omega)| \simeq |h_{a\alpha}(\omega)| \lesssim 4.7\times10^{-6}\ (\mathrm{m\,sec^{-2}})^{-1}, \quad \omega<\omega_B. \tag{B49}$$

This is completely negligible compared to the coefficients of the scale factor nonlinearity, evaluated in Eqs. (B43). Unlike the latter, however, the former cannot be reduced by means of feedback operation of the instrument. It can therefore become a dominant source of nonlinearity when a very sensitive gradiometer is operated in the force rebalance mode. Further, larger values of $h_{aa}(\omega)$ and $h_{a\alpha}(\omega)$ may arise when certain conditions from undesirable modes of the suspension springs of the proof masses which are made more compliant than the mounting structure of the gradiometer.

Experimental values for the scale factor nonlinearity coefficients can be obtained in principle from the curvature of the calibration curve of the instrument. In the calibration data displayed in Figs. 7 and 14, however, the stochastic measurement error was too large to determine a systematic departure from a linear response. Only an upper limit for $C_1^N+C_2^N$ can be obtained from Fig. 7. For an applied acceleration $g_c\simeq 4\times10^{-2}\ \mathrm{m\,sec^{-2}}$, the current response lies within 5% from the linear fit of the data. Equation (B39) then implies

$$\tfrac{1}{2}(C_1^N+C_2^N)g_c{}^2 \lesssim 0.05 g_c \tag{B50}$$

or

$$C_1^N+C_2^N \lesssim 0.1 g_c{}^{-1} = 2.5\ (\mathrm{m\,sec^{-2}})^{-1}. \tag{B51}$$

The predicted value for $C_1^N+C_2^N$, given by Eq. (B43b), is an order of magnitude smaller than this experimental limit.

Using the nonlinearity coefficients predicted by Eqs. (43), one can compute the contribution of the scale factor nonlinearity to the low-frequency noise spectrum of the gradiometer. The total common acceleration measured in the experiment is approximately

$$\int_0^\infty S_g(f')df' \lesssim 10^{-10}\ (\mathrm{m\,sec^{-2}})^2. \tag{B52}$$

Substituting this and $|h_{cc}(f)| = 0.1\ (\mathrm{m\,sec^{-2}})^{-1}$, $l=0.16$ m, $\tau=125$ sec into Eq. (B34), we find

$$[S_{\Gamma,cc}(f)]^{1/2} \lesssim 1\times10^{-2}\ \mathrm{E\,Hz^{-1/2}}\left[\frac{0.1\ \mathrm{Hz}}{f}\right]^{3/2}. \tag{B53}$$

Effects coming from terms involving $g_d(t)$ can be shown to be many orders of magnitude smaller.

D. Centrifugal acceleration

Here we consider nonlinear effects of the platform which convert external accelerations into low-frequency acceleration noise of the platform, which then couples into the gradiometer by the linear transfer function of the instrument. A well-known nonlinear mechanism of the platform is its angular motion driven by an external acceleration. The resulting centrifugal acceleration is a second-order effect.

An accelerometer mounted on the pendulum-suspended platform will experience a centrifugal acceleration $\mathbf{a}_C(t)$, in the radial direction away from the pivot point, with a magnitude

$$a_C(t) = l_p\Omega_p{}^2(t). \tag{B54}$$

For sinusoidal motions

$$\Omega_p(t) = \Omega_p\cos(\omega t/2+\theta_\Omega), \tag{B55}$$

$$a_C(t) = a_C\cos(\omega t+\theta_a)+a_{C0}, \tag{B56}$$

the amplitudes are related by

$$a_C = \tfrac{1}{2}l_p\Omega_p{}^2. \tag{B57}$$

By using Eqs. (A6b) and (A12), Ω_p can be related to the *apparent* acceleration g_F measured by the accelerometer at the fundamental frequency $f/2$:

$$\Omega_p = \frac{1}{|\hat{\mathbf{n}}\cdot(\hat{\boldsymbol{\Omega}}\times\hat{\mathbf{z}})|}\frac{Q_p}{l_p\omega_p}g_F, \tag{B58a}$$

where $\hat{\boldsymbol{\Omega}}\equiv\boldsymbol{\Omega}_p/\Omega_p$ is the unit vector along the direction of $\boldsymbol{\Omega}_p$ and $l_0=l_p$ has been assumed. Likewise, a_C can be related to the acceleration g_S measured by the accelerometer at the second harmonic f:

$$a_C = \frac{1}{|\hat{\mathbf{n}}\cdot\hat{\mathbf{z}}|}g_S. \tag{B58b}$$

Substitution of Eqs. (B58) into Eq. (B57) leads to Eq. (B37) with the identification

$$|h_N(f)| = \frac{|\hat{\mathbf{n}}\cdot\hat{\mathbf{z}}|}{|\hat{\mathbf{n}}\cdot(\hat{\boldsymbol{\Omega}}\times\hat{\mathbf{z}})|^2}\frac{Q_p{}^2}{g_E}, \tag{B59}$$

where Eq. (A1) has been used. The quantity $|h_N(f)|$ is the coefficient of *apparent nonlinearity of an accelerometer* suspended by a pendulum.

When $l_0\neq l_p$ for the accelerometer, Eq. (B58a) must be replaced by

$$\Omega_p = \frac{1}{|\hat{\mathbf{n}}\cdot(\hat{\boldsymbol{\Omega}}\times\hat{\mathbf{z}})|}\frac{1}{(1-l_0/l_p)\pi l_p f}g_F, \tag{B58a'}$$

so that

$$|h_N(f)| = \frac{|\hat{\mathbf{n}}\cdot\hat{\mathbf{z}}|}{|\hat{\mathbf{n}}\cdot(\hat{\boldsymbol{\Omega}}\times\hat{\mathbf{z}})|^2}\frac{1}{(1-l_0/l_p)^2 g_E}\left[\frac{2f_p}{f}\right]^2. \tag{B59'}$$

Therefore, the magnitude of apparent nonlinearity coefficient depends on how well the horizontal acceleration is rejected by the pendulum action.

For a gradiometer mounted on the same platform, l_p should be replaced by l in Eq. (B54) so that

$$a_C=\tfrac{1}{2}l\Omega_p{}^2 . \tag{B60}$$

With the aid of Eqs. (A6b) and (A19), Ω_p and a_C can be related to the *apparent differential acceleration* signals g_F and g_S at $f/2$ and f, respectively:

$$\Omega_p=\frac{1}{|\delta\hat{\mathbf{n}}_{+\hat{l}}|}\frac{1}{\pi l f}g_F , \tag{B61a}$$

$$a_C=\frac{1}{1-(\hat{\mathbf{n}}\cdot\hat{\boldsymbol{\Omega}})^2}g_S , \tag{B61b}$$

where $l_0=l_p$ is assumed so that the second term dominates in Eq. (A19). Substituting Eqs. (B61) into Eq. (B60), we find

$$|h_N(f)|=\frac{1-(\hat{\mathbf{n}}\cdot\hat{\boldsymbol{\Omega}})^2}{|\delta\hat{\mathbf{n}}_{+\hat{l}}|}\frac{l_p}{g_E l}\left[\frac{2f_p}{f}\right]^2 . \tag{B62}$$

This is the coefficient of *apparent nonlinearity of a gradiometer* suspended by a pendulum.

We now evaluate $|h_N(f)|$ numerically for the gravity gradiometer in the umbrella orientation for three modes of operation: (1) common accelerometer mode, (2) single accelerometer mode, and (3) gradiometer mode. For the particular orientation chosen, one finds $\hat{\mathbf{n}}\cdot\hat{\mathbf{z}}=1/\sqrt{3}$, $\hat{\mathbf{n}}\cdot\hat{\boldsymbol{\Omega}}=0$, $\hat{\mathbf{n}}\cdot(\hat{\boldsymbol{\Omega}}\times\hat{\mathbf{z}})=\sqrt{2/3}$. The condition $l_0=l_p$ is satisfied for the common mode and the gradiometer mode. For the single accelerator mode, one can show that

$$\left|1-\frac{l_0}{l_p}\right|=\frac{1}{2}(\hat{\mathbf{n}}\cdot\hat{\mathbf{z}})\frac{l}{l_p}=\frac{1}{2\sqrt{3}}\frac{l}{l_p} . \tag{B63}$$

Substituting $l=0.16$ m, $l_p=2.4$ m, $Q_p=300$, and $|\delta\hat{\mathbf{n}}_{+\hat{l}}|=7\times10^{-4}$ into Eqs. (B59), (B59′), and (B62), we obtain the theoretical predictions

$$|h_N(f)|_{th}=\begin{cases}8.0\times10^3\ (\mathrm{m\,sec^{-2}})^{-1} & \text{common accelerometer ,}\\ 2.4\times10^2(\mathrm{m\,sec^{-2}})^{-1}\left[\dfrac{2f_p}{f}\right]^2 & \text{single accelerometer ,}\\ 3.0\times10^6\ (\mathrm{m\,sec^{-2}})^{-1}\left[\dfrac{2f_p}{f}\right]^2 & \text{gradiometer .}\end{cases} \tag{B64}$$

In the experiment we were able to observe $|h_N(f)|$ at $f=2f_p$ by detecting the second harmonic amplitudes for the swinging mode of resonance frequency $f_p=0.32$ Hz. Figure 13 shows the data for the common accelerometer mode (crosses), the single accelerometer mode (dots), and the gradiometer mode (triangles). The experimental values of $|h_N(2f_p)|$ are determined from these graphs with the aid of Eq. (B37):

$$|h_N(2f_p)|_{\mathrm{expt}}=\begin{cases}5.6\times10^3\ (\mathrm{m\,sec^{-2}})^{-1} & \text{common accelerometer ,}\\ 4.6\times10^2\ (\mathrm{m\,sec^{-2}})^{-1} & \text{single accelerometer ,}\\ 4.4\times10^6\ (\mathrm{m\,sec^{-2}})^{-1} & \text{gradiometer .}\end{cases} \tag{B65}$$

Notice that all three of these values agree with the corresponding theoretical values within a factor of 2.

This excellent agreement gives us confidence that the observed second harmonics are indeed the centrifugal acceleration of the platform. Since only one parameter, $|\delta\hat{\mathbf{n}}_{+\hat{l}}|$, is relatively unknown in Eq. (B62), one can use this equation and the measured value of $|h_N(2f_p)|$ for the gradiometer to obtain a more reliable value of the misalignment:

$$|\delta\hat{\mathbf{n}}_{+\hat{l}}|=6\times10^{-4} . \tag{B66}$$

This represents a better measurement of $|\delta\hat{\mathbf{n}}_{+\hat{l}}|$ than the estimated 7×10^{-4} obtained from the observed wideband noise spectra in Sec. V C.

We now compute the low-frequency noise of the gradiometer which is generated by the centrifugal acceleration. The formalism developed in Sec. B of this appendix can be directly applied to the nonlinear equation:

$$\delta g_{d,\vec{C}}(t)=l[1-(\hat{\mathbf{n}}\cdot\hat{\boldsymbol{\Omega}})^2]\Omega_p^2(t) . \tag{B67}$$

Substituting $l[1-(\hat{\mathbf{n}}\cdot\hat{\boldsymbol{\Omega}})^2]\delta(t-t')$ into $h_N(t-t')$ and $\Omega_p(t)$ into $g(t)$, one finds the power spectral density of the centrifugal acceleration error:

$$S_{\Gamma,\vec{C}}(t)=[1-(\hat{\mathbf{n}}\cdot\hat{\boldsymbol{\Omega}})^2]\frac{2}{\pi\tau^2}\frac{1}{f^3}\left[\int_0^\infty S_\Omega(f')df'\right]^2 , \tag{B68}$$

where $S_\Omega(f')$ is the power spectral density of $\Omega_p(t)$.

For the gradiometer under pendulum suspension, Eq. (A6b) leads to

$$\int_0^\infty S_\Omega(f')df' = \frac{\tau_p}{2\pi l_p{}^2}\int_0^\infty d\omega\frac{\tau_p{}^{-1}\omega^2}{(\omega_p{}^2-\omega^2)^2+\tau_p{}^{-2}\omega^2}S_A\left[\frac{\omega}{2\pi}\right] , \tag{B69}$$

where $S_A(f)$ is the power spectral density of the horizontal acceleration $\mathbf{A}_h(t)$ *of* the pivot point. Thus, the pendulum acts as a narrow-band filter centered at f_p so that $S_A(\omega/2\pi)$ can be evaluated at f_p and taken out of the integral. The integral then has the well-known value $\pi/2$ so that

$$\int_0^\infty S_\Omega(f')df' = \frac{\tau_p}{4l_p^2} S_A(f_p) . \tag{B70}$$

Substituting this and $\hat{\mathbf{n}}\cdot\hat{\mathbf{\Omega}}=0$ into Eq. (B68), we obtain

$$S_{\Gamma,\vec{C}}(f) = \frac{1}{8\pi}\left[\frac{\tau_p}{\tau}\right]^2 \frac{1}{f^3}\left[\frac{1}{l_p^2} S_A(f_p)\right]^2 . \tag{B71}$$

When the experimental values $\tau_p=150$ sec, $\tau=125$ sec, $l_p=2.4$ m, and $S_A(f_p)=7\times10^{-13}$ $m^2 sec^{-4} Hz^{-1}$ are substituted, this yields

$$[S_{\Gamma,\vec{C}}(f)]^{1/2} = 2\times10^{-4}\ \mathrm{E\,Hz^{-1/2}} \left[\frac{0.1\ \mathrm{Hz}}{f}\right]^{3/2} . \tag{B72}$$

The derivation of this spectrum does not involve a detailed model for the apparent nonlinearity coefficient $|h_N(f)|$. Neither does it depend on the estimate of integrated acceleration noise such as Eq. (B52), since the high-frequency part of $S_A(f)$ is cut off sufficiently fast by the pendulum. Therefore, the resulting formula (B72) must give a reliable estimate of the low-frequency noise generated by the centrifugal acceleration.

*Present address: AT&T Bell Laboratories, Whippany, New Jersey 07981.

[1]P. Vanicek and E. J. Krakiwsky, *Geodesy: The Concepts* (North-Holland, Amsterdam, 1982), p. 530.

[2]T. P. Yunck, W. G. Melbourne, and C. L. Thornton, IEEE Trans. Geoscience Remote Sensing **GE-23**, 450 (1985).

[3]C. W. Misner, K. S. Thorne, and J. A. Wheeler, *Gravitation* (Freeman, San Francisco, 1973), Chap. 16.

[4]For a recent survey of the gravity gradiometer instrument development, see S. K. Jordan, in *Proceedings of the Third International Symposium on Inertial Technology for Surveying and Geodesy,* edited by K. P. Schwarz (University of Calgary Press, Canada, 1986), Vol. 2, p. 639.

[5]H. A. Chan, M. V. Moody, and H. J. Paik, Phys. Rev. Lett. **49**, 1745 (1982).

[6]H. A. Chan, M. V. Moody, H. J. Paik, and J. W. Parke, in *Proceedings of the 17th International Conference on Low Temperature Physics,* edited by U. Eckern *et al.* (North-Holland, Amsterdam, 1984), Vol. 2, p. 927.

[7]H. A. Chan, Ph.D. thesis, University of Maryland, College Park, Maryland, 1982 (unpublished).

[8]E. R. Mapoles, Ph.D. thesis, Stanford University, Stanford, California, 1981 (unpublished).

[9]H. J. Paik, Ph.D. thesis and HEPL Report No. 743, Stanford University, Stanford, California, 1974 (unpublished).

[10]K. Y. Wang, Ph.D. thesis, Stanford University, Stanford, California, 1979 (unpublished).

[11]D. G. Blair, H. J. Paik, and R. C. Taber, Rev. Sci. Instrum. **46**, 8 (1975).

[12]H. J. Paik, J. Astronaut. Sci. **29**, 1 (1981).

[13]J. W. Parke, H. J. Paik, E. R. Mapoles, W. M. Fairbank, and D. DeBra (unpublished).

[14]E. H. Metzger, in *Proceedings of AIAA Guidance and Control Specialist Conference* (Hollywood, Florida, 1977).

[15]R. L. Forward, Hughes Research Laboratories report, 1976 (unpublished).

[16]M. B. Trageser, in *Proceedings of 1st International Symposium on Inertial Technology for Surveying and Geodesy* (Canadian Institute of Surveying, Ottawa, Canada, 1977).

[17]H. A. Chan, H. J. Paik, M. V. Moody, and J. W. Parke, IEEE Trans. Magnetics **MAG-21**, 411 (1985).

[18]M. V. Moody, H. A. Chan, and H. J. Paik, J. Appl. Phys. **60**, 4308 (1986).

[19]H. A. Chan and H. J. Paik, in *Precision Measurements and Fundamental Constants II,* Natl. Bur. Stand. (U.S.) Spec. Publ. No. 617, edited by B. N. Taylor and W. D. Phillips (U.S. GPO, Washington, D.C., 1984), p. 601.

[20]H. J. Paik, IEEE Trans. Geoscience Remote Sensing **GE-23**, 524 (1985).

[21]R. L. Forward, in *Proceedings of AIAA Unmanned Spacecraft Meeting* (AIAA, Los Angeles, California, 1965), p. 346.

[22]M. Schwartz, *Information, Transmission, Modulation, and Noise* (McGraw-Hill, New York, 1980), p. 348.

[23]M. V. Moody, H. A. Chan, H. J. Paik, and C. Stephens, in *Proceedings of the 17th International Conference on Low Temperature Physics* (Ref. 6), Vol. 1, p. 407.

[24]S. O. Rice, in *Selected Papers on Noise and Stochastic Processes,* edited by N. Wax (Dover, New York, 1954), pp. 264 and 293.

[25]J. S. Bendat and A. G. Piersol, *Random Data: Analysis and Measurement Procedures* (Wiley, New York, 1971), pp. 74, 81, and 320.

[26]D. Sonnabend, Engineering Memo 314-388, Jet Propulsion Laboratory, Pasedena, California, 1986 (unpublished).